Nonequilibrium Steady-State Transport in Quantum Impurity Models: A Thermofield and Quantum Quench Approach Using Matrix Product States

F. Schwarz,[1] I. Weymann,[2] J. von Delft,[1] and A. Weichselbaum[1,3,*]

[1]*Physics Department, Arnold Sommerfeld Center for Theoretical Physics, and Center for NanoScience, Ludwig-Maximilians-Universität, Theresienstraße 37, 80333 München, Germany*

[2]*Faculty of Physics, Adam Mickiewicz University, Umultowska 85, 61-614 Poznań, Poland*

[3]*Department of Condensed Matter Physics and Materials Science, Brookhaven National Laboratory, Upton, New York 11973-5000, USA*

The numerical renormalization group (NRG) is tailored to describe interacting impurity models in equilibrium, but it faces limitations for steady-state nonequilibrium, arising, e.g., due to an applied bias voltage. We show that these limitations can be overcome by describing the thermal leads using a thermofield approach, integrating out high energy modes using NRG, and then treating the nonequilibrium dynamics at low energies using a quench protocol, implemented using the time-dependent density matrix renormalization group. This yields quantitatively reliable results for the current (with errors $\lesssim 3\%$) down to the exponentially small energy scales characteristic of impurity models. We present results of benchmark quality for the temperature and magnetic field dependence of the zero-bias conductance peak for the single-impurity Anderson model.

Introduction.—A major open problem in the theoretical study of nanostructures, such as quantum dots or nanowires, is the reliable computation of the nonlinear conductance under the conditions of nonequilibrium steady-state (NESS) transport. These are open quantum systems featuring strong local interactions, typically described by quantum impurity models such as the interacting resonant level model (IRLM), the Kondo model (KM), or the single-impurity Anderson model (SIAM). Much work has been devoted to studying the NESS properties of such models using a variety of methods [1–15], leading to a fairly good qualitative understanding of their behavior. The interplay of strong correlations, NESS driving, and dissipative effects leads to a rich and complex phenomenology. In particular, for the KM and SIAM, the nonlinear conductance exhibits a striking zero-bias peak, the so-called Kondo peak, characterized by a small energy scale, the Kondo temperature T_K, that weakens with increasing temperature and splits with increasing magnetic field, in qualitative agreement with experiments [16–22]. However, a full, quantitative description of the NESS behavior of such models under generic conditions has so far been unfeasible: none of the currently available approaches meet the three-fold challenge of (i) treating interactions essentially exactly, (ii) resolving very small energy scales, and (iii) incorporating NESS conditions.

This Letter presents an approach that does meet this challenge. (i) To deal with interactions, we use numerical matrix product state (MPS) methods. (ii) We use the numerical renormalization group (NRG) [23,24] to integrate out high-energy modes, leading to a renormalized impurity

problem [25] whose reduced effective bandwidth, D^*, is set by a transport window defined by the voltage bias (V) and the temperature (T). This considerably enlarges the window of accessible time scales, which scale as $1/D^*$, and thus it enables us to treat arbitrary voltages. (iii) We then study the transport properties of the renormalized problem using a quench protocol where we abruptly switch on the impurity-lead coupling and compute the subsequent time evolution of the current, $J(t)$, using the time-dependent density-matrix renormalization group (TDMRG) [26–29]. Whereas similar
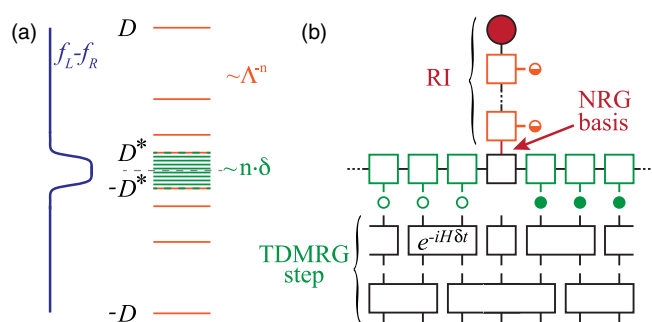

FIG. 1. (a) The discretization combines a log-sector for high energy excitations with a lin-sector for the TW. (b) The log-sector is treated using NRG. Here, "holes" and "particles" are recombined. The effective low-energy basis of NRG is used as the local state space of one MPS chain element. For the lin-sector, holes (empty at $t = 0$) and particles (filled at $t = 0$) are treated separately. On the chain including the RI, we do a TDMRG calculation based on a Trotter decomposition in "odd" and "even" bonds [37].

protocols [5,15,30,31] typically work at $T = 0$, we consider nonequilibrium thermal leads for arbitrary T, using the thermofield approach [32–36] to describe them with a pure product state in an enlarged Hilbert space.

We benchmark our approach using the IRLM, finding excellent agreement with exact Bethe-ansatz predictions for the NESS current. We then turn to the SIAM. For the linear conductance, we reproduce equilibrium NRG results. For the nonlinear conductance, we study the evolution of the zero-bias peak with T and magnetic field.

Setup.—We consider impurities coupled to two thermal leads, labeled $\alpha \in \{L, R\}$ and characterized by Fermi functions $f_\alpha(\omega) = (e^{(\omega - \mu_\alpha)/T} + 1)^{-1}$, where $\mu_{L/R} = \pm V/2$. (We set $e = \hbar = k_B = 1$.) We study two different models, the spinless IRLM with a three-site impurity and Coulomb repulsion U between neighboring sites, and the SIAM with Coulomb repulsion U between different spins and a Zeeman splitting due to a magnetic field B. The impurities of these models are described by

$$H_{\text{imp}}^{(I)} = \varepsilon_d \hat{n}_C + U(\hat{n}_L + \hat{n}_R - 1)\hat{n}_C$$
$$+ (t' d_C^\dagger d_L + t' d_C^\dagger d_R + \text{H.c.}) \qquad (1)$$

$$H_{\text{imp}}^{(S)} = \varepsilon_d(\hat{n}_{d\uparrow} + \hat{n}_{d\downarrow}) + U\hat{n}_{d\uparrow}\hat{n}_{d\downarrow} - \frac{B}{2}(\hat{n}_{d\uparrow} - \hat{n}_{d\downarrow}), \qquad (2)$$

where $\hat{n}_i = d_i^\dagger d_i$, for $i \in \{L, R, C, d\uparrow, d\downarrow\}$. In this Letter, we focus on the particle-hole symmetric case ($\varepsilon_d = 0$ for the IRLM and $\varepsilon_d = -(U/2)$ for the SIAM). The leads are assumed to be noninteracting,

$$H_{\text{lead}}^{(I/S)} = \sum_{\alpha(\sigma)k} \varepsilon_k c_{\alpha(\sigma)k}^\dagger c_{\alpha(\sigma)k} \equiv \sum_q \varepsilon_q c_q^\dagger c_q, \qquad (3)$$

with spin index $\sigma \in \{\uparrow, \downarrow\}$ for the SIAM, $q \equiv \{\alpha, (\sigma), k\}$ a composite index, and k a label for the energy levels. The impurity-leads hybridization is given by

$$H_{\text{hyb}}^{(I/S)} = \sum_q (v_q d_{\alpha/\sigma}^\dagger c_q + \text{H.c.}), \qquad (4)$$

where in the IRLM the left (right) impurity site d_L (d_R) couples to the modes c_{Lk} (c_{Rk}), respectively, while in the SIAM the two spin states d_σ couple to the lead modes $c_{\alpha\sigma k}$ spin-independently, $v_q = v_{\alpha k}$. The couplings v_q induce an impurity-lead hybridization $\Gamma_\alpha(\omega) = \pi \sum_{k\sigma} |v_q|^2 \delta(\omega - \varepsilon_q)$, chosen such that they represent a box distribution $\Gamma_\alpha(\omega) = \Gamma_\alpha \Theta(D - |\omega|)$ in the continuum limit with half-bandwidth $D := 1$ set as the unit of energy, unless specified otherwise. For the IRLM, we set $\Gamma_L = \Gamma_R = 0.5D$ corresponding to the hopping element of a tight-binding chain with half-bandwidth D, and for the SIAM, we likewise choose $\Gamma_L = \Gamma_R$ and define the total hybridization $\Gamma = \Gamma_L + \Gamma_R$.

Strategy.—We describe the thermal leads decoupled from the impurity using the thermofield approach [32–35]. The impurity-lead coupling induces nonequilibrium processes, which occur on energy scales corresponding to the *transport window* (TW), defined as the energy range in which $f_L(\omega) \approx f_R(\omega)$. Energy scales far outside of this TW are effectively in equilibrium, and we therefore integrate them out using NRG, whereas we describe the nonequilibrium physics within the TW using TDMRG quench. We implement both the NRG and TDMRG using MPS techniques. We use a logarithmically discretized sector (log-sector), representing the energy range of the leads outside of the TW, and a linearly discretized sector (lin-sector) within the TW, as depicted in Fig. 1(a). The transition from the logarithmic to the linear discretization can be smoothed [37]. To simplify the MPS calculation, we map the leads onto a chain, with on-site and nearest-neighbor terms only, by tridiagonalizing the Hamiltonian. Integrating out the log-sector using NRG we get a *renormalized impurity* (RI) [25] and a reduced effective bandwidth, $2D^*$, of order of the size of the TW. This enables us to treat transport on energy scales much smaller than D. In particular, we can study arbitrary ratios of V/T_K in the SIAM, even if $T_K \ll D$. We then turn on the coupling between the log-sector and lin-sector by performing a TDMRG quench, starting from an initial state $|\Psi_{\text{ini}}\rangle = |\phi_{\text{ini}}\rangle \otimes |\Omega_{\text{lin}}\rangle$, where $|\phi_{\text{ini}}\rangle$ describes the initial state of the RI, and $|\Omega_{\text{lin}}\rangle$ is a *pure product state* describing the lin-sector of the thermal leads in the thermofield approach. To describe steady-state properties, we time-evolve $|\Psi_{\text{ini}}\rangle$ until expectation values are stationary up to oscillations around their mean value. Since the effective bandwidth relevant for this TDMRG calculation is given by D^*, not D, exponentially large time scales of order $1/D^* \gg 1/D$ are accessible.

Thermofield description of decoupled leads.—In the context of MPS methods, the thermofield description [32–35] of the decoupled leads has two advantages: finite temperature states are represented as pure states, and thermal leads are described by a simple product state.

Akin to purification [29], we double our Hilbert space by introducing one auxiliary mode c_{q2} (not coupled to the system) for each lead mode $c_{q1} = c_q$. In this enlarged Hilbert space, we define a pure state $|\Omega\rangle$ such that the thermal expectation value of an operator A acting on the original physical lead is given by $\langle A \rangle = \langle \Omega | A | \Omega \rangle$. This state can be written as [37]

$$|\Omega\rangle = \prod_q \underbrace{\left(\sqrt{1 - f_q}|0, 1\rangle_q + \sqrt{f_q}|1, 0\rangle_q\right)}_{\equiv |\tilde{0}, \tilde{1}\rangle_q}, \qquad (5)$$

with $f_q = f_\alpha(\varepsilon_q)$, where $|0, 1\rangle_q$ and $|1, 0\rangle_q$ are defined by $c_{q1}|0, 1\rangle_q = c_{q2}^\dagger|0, 1\rangle_q = c_{q1}^\dagger|1, 0\rangle_q = c_{q2}|1, 0\rangle_q = 0$ for all q. We map $|\Omega\rangle$ to a pure product state using the rotation

$$\begin{pmatrix} \tilde{c}_{q1} \\ \tilde{c}_{q2} \end{pmatrix} = \begin{pmatrix} \sqrt{1-f_q} & -\sqrt{f_q} \\ \sqrt{f_q} & \sqrt{1-f_q} \end{pmatrix} \begin{pmatrix} c_{q1} \\ c_{q2} \end{pmatrix}. \quad (6)$$

Having $\tilde{c}_{q1}|\Omega\rangle = \tilde{c}_{q2}^\dagger|\Omega\rangle = 0$, the modes $\tilde{c}_{q1}$ ($\tilde{c}_{q2}$) can be interpreted as holes (particles) which are empty (filled) in the thermal state, respectively. Since in Eq. (5) we constructed $|\Omega\rangle$ to be an eigenstate of the particle number operator, it remains so in the rotated basis. The physical and auxiliary modes are decoupled in the unrotated basis; hence we are free to choose an arbitrary Hamiltonian (and hence time evolution) for the auxiliary modes [47]. We choose their single-particle energies equal to those of the physical modes, $\varepsilon_{q2} = \varepsilon_q$, in order to ensure that the resulting total lead Hamiltonian is diagonal in j in both the original *and* the rotated basis:

$$\mathcal{H}_{\text{lead}} \equiv H_{\text{lead}} + H_{\text{aux}} = \sum_{qj}\varepsilon_q c_{qj}^\dagger c_{qj} = \sum_{qj}\varepsilon_q \tilde{c}_{qj}^\dagger \tilde{c}_{qj}. \quad (7)$$

Equation (4) is rotated into $H_{\text{hyb}}^{(\text{I/S})} = \sum_{qj}(\tilde{v}_{qj}d_{\alpha/\sigma}^\dagger \tilde{c}_{qj} + \text{H.c.})$, whose couplings, $\tilde{v}_{q1} = v_q\sqrt{1-f_q}$ and $\tilde{v}_{q2} = v_q\sqrt{f_q}$, now *explicitly depend* on the Fermi function and encode all relevant information about temperature and voltage.

For the SIAM, we use a specific linear combination of $\tilde{c}_{Lk\sigma i}$ and $\tilde{c}_{Rk\sigma i}$ modes, $\tilde{C}_{k\sigma i} \propto \sum_\alpha \tilde{v}_{\alpha k\sigma i}\tilde{c}_{\alpha k\sigma i}$, because the modes orthogonal to these [37] decouple. Mixing left and right lead modes is possible despite the nonequilibrium situation, because the difference in chemical potentials is accounted for by the V-dependent couplings $\tilde{v}_q$. In the IRLM, this reduction of modes is not possible because left and right lead couple to different impurity sites.

NRG renormalization of the impurity.—As is standard for NRG, we map the leads (in the thermofield representation) from the original "star geometry" to a chain geometry. To ensure that $|\Omega\rangle$ remains a product state, we perform the corresponding unitary transformation for holes and particles independently. This results in a chain consisting of two channels $i \in \{1,2\}$ for the SIAM, and four for the IRLM due to the additional lead index $\alpha \in \{L, R\}$. The first part of the chain corresponds to the log-sector, the later part to the lin-sector. The hoppings within the log-sector decay as Λ^{-n}, because for each lead level q within the log-sector of the original star geometry, either $\tilde{c}_{q1}$ or $\tilde{c}_{q2}$ decouples from the RI due to $f_q \in \{0, 1\}$. For NRG calculations, it is unfavorable to describe holes and particles in separate chains, because then particle-hole excitations involve opposite levels of different chains. For that reason, we recombine the holes and particles of the log-sector into one chain using a further tridiagonalization. In the IRLM, this is done for each lead α independently. After that, the log-sector resembles a standard Wilson chain with hoppings that scale as $\Lambda^{-n/2}$, reflecting the fact that the log-sector is

effectively in equilibrium. A sketch of the different geometries can be found in Fig. S2 of Ref. [37].

Using NRG, we find an effective low-energy many-body basis for the log-sector, which we interpret as the local state space of a RI, and we treat it as one chain element of our MPS chain. Coupled to this RI, we have the lin-sector of the leads, represented as two separate chains for holes and particles, as shown in the upper part of Fig. 1(b).

TDMRG quench.—We choose the initial state for the quench as the product state $|\Psi_{\text{ini}}\rangle = |\phi_{\text{ini}}\rangle \otimes |\Omega_{\text{lin}}\rangle$. This implies that for the lin-sector, we start with the state in which all holes (particles) are empty (filled). As the initial state of the RI, $|\phi_{\text{ini}}\rangle$, we choose a ground state of the NRG basis (in principle, one can choose any of the low-energy basis states whose excitation energy is well within the TW). We then switch on the coupling between the RI and the leads, smoothly over a short time window. The system time-evolves under the Hamiltonian $\hat{H} = H_{\text{imp}} + H_{\text{hyb}} + H_{\text{lead}} + H_{\text{aux}}$, $|\Psi(t)\rangle = e^{-i\hat{H}t}|\Psi_{\text{ini}}\rangle$. We perform the time evolution using TDMRG based on a second order Trotter decomposition, as depicted in Fig. 1(b), with a Trotter time step of order $1/D^*$. (Technical details can be found in Sec. S-3.C of Ref. [37].) The fact that this initial lead state is entanglement-free is advantageous for reaching comparatively long times. We extract NESS information from $\langle A(t)\rangle = \langle\Psi(t)|A|\Psi(t)\rangle$ within a window of intermediate times, large enough for post-quench transients to no longer dominate, but well below the recurrence time, where finite-size effects set in. We compute the current through the impurity site (SIAM) or the central impurity site (IRLM), respectively, using $J = \frac{1}{2}(J_L - J_R)$, where J_L (J_R) is the current that flows into the site from the left (right), respectively [37]. We are able to track the time evolution up to times of order $1/D^*$. Since $D^* \sim \max(V, T)$, this suffices to describe particle transport for any choice of V or T. However, processes on much smaller energy scales cannot necessarily be resolved (see Sec. S-4.C of [37] for details).

Interacting resonant level model.—We benchmark our method for the IRLM, for which Ref. [15] computed the steady-state current at $T = 0$ both numerically, using DMRG quenches, and analytically, using the exact Bethe ansatz. A universal scaling of the current-voltage characteristics was found at the self-dual point of the model, with the corresponding energy scale T_B scaling as $(t')^{3/4}$. (These results were very recently confirmed by Ref. [48].) Figure 2 presents a comparison of our data with the analytical expression for the universal scaling curve given in [15], for the current as function of voltage at $T = 0$ at the self-dual point $U \approx D$ and $\varepsilon_d = 0$. The agreement is excellent for a large range of t' values. For each value of t', T_B was used as a fit parameter; the resulting T_B values, shown in the inset, agree nicely with the scaling predicted in [15]. Using the fitted values of T_B, all data points deviate by less than 2% from the Bethe results. Our use of NRG to renormalize
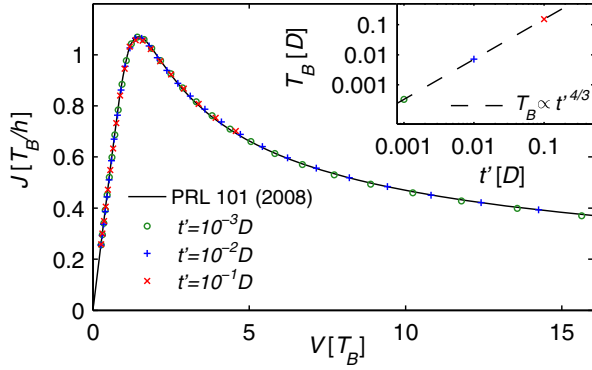
FIG. 2. Universal scaling of current vs voltage for the IRLM at the self-dual point for $T = 0$, in units of the energy scale $T_B(t')$, with negative differential conductance at large voltages, in excellent agreement with analytical results (solid curve, [15]). The inset shows the scaling of T_B with $(t')^{3/4}$.

the impurity enables us to study values of t' up to a hundred times smaller than the values used in [15], giving us access to much smaller values of T_B and larger V/T_B ratios.

Single-impurity Anderson model.—For the SIAM, a natural first check is the noninteracting case, $U = 0$, which is exactly solvable, but its treatment in MPS numerics does not differ from the case $U \neq 0$. The inset of Fig. 3(a) displays the current over voltage for two different temperatures, showing good agreement between our MPS numerics and exact predictions, thus providing direct evidence for the validity of our approach. For $U \neq 0$, our method yields quantitative agreement with previous numerical results obtained in the regime $V \gtrsim \Gamma$ [6,7], see Sec. S-6 of Ref. [37] for details. Furthermore, we find good agreement with the auxiliary master equation approach for arbitrary voltages, see Ref. [49] for details.

The main panel of Fig. 3(a) focuses on the differential conductance $g(T, V) = (\partial J(T, V)/\partial V)/(2e^2/h)$ for strong interactions. As a consistency check, we compare our results for $g(T, 0)$ with the linear conductance computed using FDM-NRG [51]. We find excellent agreement over a large range of temperatures. From this data, we define the Kondo temperature T_K via the condition $g(T_K, 0) \equiv \frac{1}{2}$.

We also show $g(0, V)$ over a wide voltage range in Fig. 3(a). In agreement with experiment [22] and other theoretical work [8], this curve lies above $g(T, 0)$. The difference can be quantified by the value of $g(0, T_K)$, a universal number characterizing NESS transport for the SIAM, whose precise value is not yet known with quantitative certainty. Our method, which we trust to be quantitatively reliable, yields $g(0, T_K) \approx 0.60 \pm 0.02$ in the Kondo limit of $U/\Gamma \gg 1$, where the estimated error bar of about 3% is likely conservative (cf. [37]). For comparison, (nonexact) analytical calculations for the Kondo model yielded $g(0, T_K) \approx 2/3$ [8,9].

Figures 3(b)–3(d) show our quantitative description of the T- and B-dependence of the zero-bias peak in the Kondo limit ($U/\Gamma = 12$). With increasing T at $B = 0$, the zero-bias peak decreases [Fig. 3(b)], as observed in numerous experiments [17–22]. For finite B, the zero-bias peak splits into two sub-peaks at $V \approx \pm B$ [Fig. 3(c)]. A more detailed analysis of the value of B, at which the peak begins to split [52,53], is given in Sec. S-7 of Ref. [37]. In Fig. 3(d), the peak position with respect to B is resolved in more detail, with the voltage given in units of B. While for $B \approx 2T_K$ the peak position is roughly at $V/B \approx 0.83$, it quickly tends towards $V/B = 1$ for larger magnetic fields. Our study thus quantitatively confirms that the large-field peak-to-peak splitting for the nonlinear conductance is $\approx 2B$, as observed in several experiments [16,17,20]. This is also found in independent calculations [49] using the approach of Ref. [13].
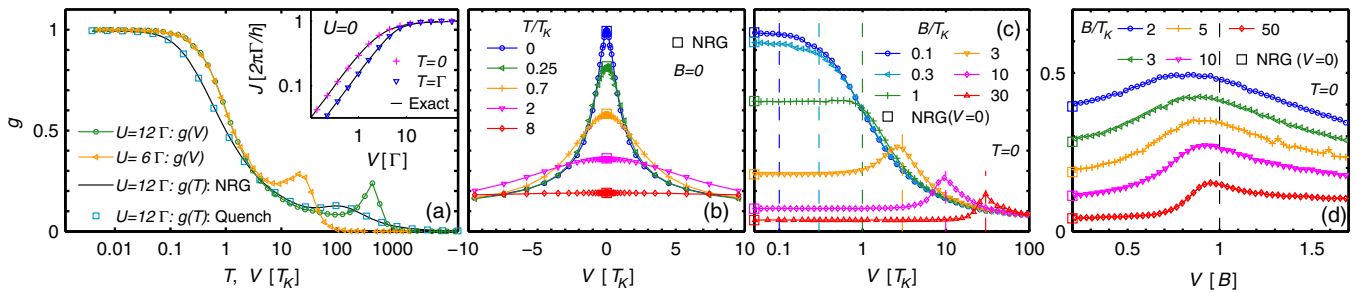

FIG. 3. Numerical results for the SIAM with $\Gamma = 10^{-3}$. For $U = 12\Gamma$, used in (b)–(d), we find $T_K = 2.61 \times 10^{-5}$. [This implies $T_K = 1.04 T_K^{(\chi)}$, where $T_K^{(\chi)} = (1/4\chi_s) = (U\Gamma/2)^{\frac{1}{2}} e^{\pi[(\Gamma/2U)-(U/8\Gamma)]}$ is an alternative definition of the Kondo temperature based on the Bethe-ansatz result [50] for the static spin susceptibility χ_s, at $B = T = 0$]. (a) Conductance vs V and T: squares show quench results in linear response as function of T, $g(T, 0)$, in good agreement with the NRG results (solid line). Dots and triangles show quench results for the nonlinear conductance vs V at $T = 0$ for two different values of U. Inset: current vs V for $U = 0$ on a log-log scale, for two different temperatures, showing excellent agreement with analytical results. (b) Disappearance of the Kondo resonance in $g(T, V)$ with increasing T at $B = 0$, with $g(T, -V) = g(T, V)$, by symmetry. (c) Splitting of the resonance in $g(0, V)$ for finite B. Two subpeaks emerge at $V \approx \pm B$, as marked by the dashed lines. (d) Similar data as in (c) but plotted vs V/B and on a linear scale. For $B = 2T_K$, the peak position in the conductance $g(0, V)$ is still slightly below B, but for a higher magnetic field, the peak clearly moves towards $V/B \approx 1$. In (b)–(d), the squares indicate the NRG result for $V = 0$.

Summary and outlook.—We have combined the thermo-field approach with a hybrid NRG-TDMRG quench strategy to reach a longstanding goal: a versatile, flexible, and *quantitatively reliable* method for studying quantum impurity models in steady-state nonequilibrium. Because of these features, our scheme has the potential of developing into the method of choice for such settings, in the same way as NRG is the method of choice for equilibrium impurity models. Indeed, various quantitative benchmark tests have confirmed the accuracy of our scheme, and it can easily be applied to other models and setups. For example, a generalization to a finite temperature difference between the left and right lead would be straightforward. It would also be interesting to use our setup for quantitative studies of the nonequilibrium two-channel Kondo physics measured in [54], or to study impurity models with superconducting leads, since the hybrid NRG-TDMRG approach is ideally suited for dealing with the bulk gap.

Methodologically, our setup can straightforwardly be extended to study NESS physics, without resorting to a quench strategy, by including Lindblad driving terms in the Liouville equation, which are *local* on the MPS chain [55]. Although the direct time-evolution of such Lindblad equations based on tensor networks seems feasible [56], one could try to avoid the real-time evolution altogether, and target the steady-state directly, by looking for the density matrix that fulfills $\dot{\rho} = 0$ [57,58].

[*] andreas.weichselbaum@lmu.de

[1] A. Rosch, J. Paaske, J. Kroha, and P. Wölfle, Nonequilibrium Transport Through a Kondo Dot in a Magnetic Field: Perturbation Theory and Poor Man's Scaling, Phys. Rev. Lett. **90,** 076804 (2003).

[2] S. Kehrein, Scaling and Decoherence in the Nonequilibrium Kondo Model, Phys. Rev. Lett. **95,** 056602 (2005).

[3] F. B. Anders, Steady-State Currents Through Nanodevices: A Scattering-States Numerical Renormalization-Group Approach to Open Quantum Systems, Phys. Rev. Lett. **101,** 066804 (2008).

[4] S. Kirino, T. Fujii, J. Zhao, and K. Ueda, Time-dependent DMRG study on quantum dot under a finite bias voltage, J. Phys. Soc. Jpn. **77,** 084704 (2008).

[5] F. Heidrich-Meisner, A. E. Feiguin, and E. Dagotto, Real-time simulations of nonequilibrium transport in the single-impurity Anderson model, Phys. Rev. B **79,** 235336 (2009).

[6] J. Eckel, F. Heidrich-Meisner, S. G. Jakobs, M. Thorwart, M. Pletyukhov, and R. Egger, Comparative study of theoretical methods for non-equilibrium quantum transport, New J. Phys. **12,** 043042 (2010).

[7] P. Werner, T. Oka, M. Eckstein, and A. J. Millis, Weak-coupling quantum Monte Carlo calculations on the Keldysh contour: Theory and application to the current-voltage characteristics of the Anderson model, Phys. Rev. B **81,** 035108 (2010).

[8] M. Pletyukhov and H. Schoeller, Nonequilibrium Kondo Model: Crossover from Weak to Strong Coupling, Phys. Rev. Lett. **108,** 260601 (2012).

[9] S. Smirnov and M. Grifoni, Keldysh effective action theory for universal physics in spin-$\frac{1}{2}$ Kondo dots, Phys. Rev. B **87,** 121302 (2013).

[10] G. Cohen, E. Gull, D. R. Reichman, and A. J. Millis, Green's Functions from Real-Time Bold-Line Monte Carlo Calculations: Spectral Properties of the Nonequilibrium Anderson Impurity Model, Phys. Rev. Lett. **112,** 146802 (2014).

[11] A. E. Antipov, Q. Dong, and E. Gull, Voltage Quench Dynamics of a Kondo System, Phys. Rev. Lett. **116,** 036801 (2016).

[12] F. Reininghaus, M. Pletyukhov, and H. Schoeller, Kondo model in nonequilibrium: Interplay between voltage, temperature, and crossover from weak to strong coupling, Phys. Rev. B **90,** 085121 (2014).

[13] A. Dorda, M. Ganahl, H. G. Evertz, W. von der Linden, and E. Arrigoni, Auxiliary master equation approach within matrix product states: Spectral properties of the nonequilibrium Anderson impurity model, Phys. Rev. B **92,** 125145 (2015).

[14] S. G. Jakobs, V. Meden, and H. Schoeller, Nonequilibrium Functional Renormalization Group for Interacting Quantum Systems, Phys. Rev. Lett. **99,** 150603 (2007).

[15] E. Boulat, H. Saleur, and P. Schmitteckert, Twofold Advance in the Theoretical Understanding of far-from-Equilibrium Properties of Interacting Nanostructures, Phys. Rev. Lett. **101,** 140601 (2008).

[16] D. C. Ralph and R. A. Buhrman, Kondo-Assisted and Resonant Tunneling via a Single Charge Trap: A Realization of the Anderson Model Out of Equilibrium, Phys. Rev. Lett. **72,** 3401 (1994).

[17] D. Goldhaber-Gordon, H. Shtrikman, D. Mahalu, D. Abusch-Magder, U. Meirav, and M. A. Kastner, Kondo effect in a single-electron transistor, Nature (London) **391,** 156 (1998).

[18] S. M. Cronenwett, T. H. Oosterkamp, and L. P. Kouwenhoven, A tunable Kondo effect in quantum dots, Science **281,** 540 (1998).

[19] F. Simmel, R. H. Blick, J. P. Kotthaus, W. Wegscheider, and M. Bichler, Anomalous Kondo Effect in a Quantum Dot at Nonzero Bias, Phys. Rev. Lett. **83,** 804 (1999).

[20] W. G. van der Wiel, S. D. Franceschi, T. Fujisawa, J. M. Elzerman, S. Tarucha, and L. P. Kouwenhoven, The Kondo effect in the unitary limit, Science **289,** 2105 (2000).

[21] A. V. Kretinin, H. Shtrikman, D. Goldhaber-Gordon, M. Hanl, A. Weichselbaum, J. von Delft, T. Costi, and D. Mahalu, Spin-$\frac{1}{2}$ Kondo effect in an InAs nanowire quantum dot: Unitary limit, conductance scaling, and Zeeman splitting, Phys. Rev. B **84,** 245316 (2011).

[22] A. V. Kretinin, H. Shtrikman, and D. Mahalu, Universal line shape of the Kondo zero-bias anomaly in a quantum dot, Phys. Rev. B **85**, 201301 (2012).

[23] K. G. Wilson, The renormalization group: Critical phenomena and the Kondo problem, Rev. Mod. Phys. **47**, 773 (1975).

[24] R. Bulla, T. A. Costi, and T. Pruschke, Numerical renormalization group method for quantum impurity systems, Rev. Mod. Phys. **80**, 395 (2008).

[25] F. Güttge, F. B. Anders, U. Schollwöck, E. Eidelstein, and A. Schiller, Hybrid NRG-DMRG approach to real-time dynamics of quantum impurity systems, Phys. Rev. B **87**, 115115 (2013).

[26] G. Vidal, Efficient Simulation of One-Dimensional Quantum Many-Body Systems, Phys. Rev. Lett. **93**, 040502 (2004).

[27] A. J. Daley, C. Kollath, U. Schollwöck, and G. Vidal, Time-dependent density-matrix renormalization-group using adaptive effective Hilbert spaces, J. Stat. Mech. (2004) P04005.

[28] S. R. White and A. E. Feiguin, Real-Time Evolution Using the Density Matrix Renormalization Group, Phys. Rev. Lett. **93**, 076401 (2004).

[29] U. Schollwöck, The density-matrix renormalization group in the age of matrix product states, Ann. Phys. (Amsterdam) **326**, 96 (2011).

[30] A. Branschädel, G. Schneider, and P. Schmitteckert, Conductance of inhomogeneous systems: Real-time dynamics, Ann. Phys. (Amsterdam) **522**, 657 (2010).

[31] L. G. G. V. D. da Silva, F. Heidrich-Meisner, A. E. Feiguin, C. A. Büsser, G. B. Martins, E. V. Anda, and E. Dagotto, Transport properties and Kondo correlations in nanostructures: Time-dependent DMRG method applied to quantum dots coupled to Wilson chains, Phys. Rev. B **78**, 195317 (2008).

[32] Y. Takahashi and H. Umezawa, Thermo field dynamics, Collective Phenomena **2**, 55 (1975).

[33] S. M. Barnett and B. J. Dalton, Liouville space description of thermofields and their generalisations, J. Phys. A **20**, 411 (1987).

[34] A. Das, Topics in finite temperature field theory," in *Quantum Field Theory—A 20th Century Profile*, edited by A. N. Mitra (Hindustan Book Agency, New Delhi, 2000) pp. 383–411.

[35] I. de Vega and M.-C. Bañuls, Thermofield-based chain-mapping approach for open quantum systems, Phys. Rev. A **92**, 052116 (2015).

[36] C. Guo, I. de Vega, U. Schollwöck, and D. Poletti, Stable-unstable transition for a Bose-Hubbard chain coupled to an environment, Phys. Rev. A **97**, 053610 (2018),

[37] See Supplemental Material at http://link.aps.org/supplemental/10.1103/PhysRevLett.121.137702, which includes Refs. [38–46], for details.

[38] V. L. Campo and L. N. Oliveira, Alternative discretization in the numerical renormalization-group method, Phys. Rev. B **72**, 104432 (2005).

[39] R. Žitko, Adaptive logarithmic discretization for numerical renormalization group methods, Comput. Phys. Commun. **180**, 1271 (2009).

[40] A. Weichselbaum, Discarded weight and entanglement spectra in the numerical renormalization group, Phys.

[41] Rev. B **84**, 125130 (2011); Tensor networks and the numerical renormalization group, Phys. Rev. B **86**, 245124 (2012); Non-Abelian symmetries in tensor networks: A quantum symmetry space approach, Ann. Phys. (Amsterdam) **327**, 2972 (2012).

[41] P. Corboz, R. Orús, B. Bauer, and G. Vidal, Simulation of strongly correlated fermions in two spatial dimensions with fermionic projected entangled-pair states, Phys. Rev. B **81**, 165104 (2010).

[42] G. Schneider and P. Schmitteckert, Conductance in strongly correlated 1D systems: Real-time dynamics in DMRG, arXiv:cond-mat/0601389.

[43] P. Wang and S. Kehrein, Flow equation calculation of transient and steady-state currents in the Anderson impurity model, Phys. Rev. B **82**, 125124 (2010).

[44] T. Barthel, U. Schollwöck, and S. R. White, Spectral functions in one-dimensional quantum systems at finite temperature using the density matrix renormalization group, Phys. Rev. B **79**, 245101 (2009).

[45] P. Schmitteckert, Calculating Green functions from finite systems, J. Phys. Conf. Ser. **220**, 012022 (2010).

[46] M. Hanl and A. Weichselbaum, Local susceptibility and Kondo scaling in the presence of finite bandwidth, Phys. Rev. B **89**, 075130 (2014).

[47] C. Karrasch, J. H. Bardarson, and J. E. Moore, Finite-temperature dynamical density matrix renormalization group and the Drude weight of spin-1/2 chains, Phys. Rev. Lett. **108**, 227206 (2012).

[48] K. Bidzhiev and G. Misguich, Out-of-equilibrium dynamics in a quantum impurity model: Numerics for particle transport and entanglement entropy, Phys. Rev. B **96**, 195117 (2017).

[49] D. M. Fugger, A. Dorda, F. Schwarz, J. von Delft, and E. Arrigoni, Nonequilibrium Kondo effect in a magnetic field: auxiliary master equation approach, New J. Phys. **20**, 013030 (2018).

[50] P. B. Wiegmann and A. M. Tsvelick, Exact solution of the Anderson model: I, J. Phys. C **16**, 2281 (1983); A. M. Tsvelick and P. B. Wiegmann, Exact solution of the Anderson model. II. Thermodynamic properties at finite temperatures, J. Phys. C **16**, 2321 (1983).

[51] A. Weichselbaum and J. von Delft, Sum-Rule Conserving Spectral Functions from the Numerical Renormalization Group, Phys. Rev. Lett. **99**, 076402 (2007).

[52] M. Filippone, C. P. Moca, A. Weichselbaum, J. von Delft, and C. Mora, At which magnetic field, exactly, does the Kondo resonance begin to split? a Fermi liquid description of the low-energy properties of the Anderson model, Phys. Rev. B **98**, 075404 (2018).

[53] A. Oguri and A. C. Hewson, Higher-Order Fermi-Liquid Corrections for an Anderson Impurity Away from Half Filling, Phys. Rev. Lett. **120**, 126802 (2018); Higher-order Fermi-liquid corrections for an Anderson impurity away from half filling: Equilibrium properties, Phys. Rev. B **97**, 045406 (2018); Higher-order Fermi-liquid corrections for an Anderson impurity away from half filling: Nonequilibrium transport, Phys. Rev. B **97**, 035435 (2018).

[54] Z. Iftikhar, S. Jezouin, A. Anthore, U. Gennser, F. D. Parmentier, A. Cavanna, and F. Pierre, Two-channel Kondo

effect and renormalization flow with macroscopic quantum charge states, Nature (London) **526**, 233 (2015).

[55] F. Schwarz, M. Goldstein, A. Dorda, E. Arrigoni, A. Weichselbaum, and J. von Delft, Lindblad-driven discretized leads for nonequilibrium steady-state transport in quantum impurity models: Recovering the continuum limit, Phys. Rev. B **94**, 155142 (2016).

[56] A. H. Werner, D. Jaschke, P. Silvi, M. Kliesch, T. Calarco, J. Eisert, and S. Montangero, Positive Tensor Network Approach for Simulating Open Quantum Many-Body Systems, Phys. Rev. Lett. **116**, 237201 (2016).

[57] J. Cui, J. I. Cirac, and M. C. Bañuls, Variational Matrix Product Operators for the Steady State of Dissipative Quantum Systems, Phys. Rev. Lett. **114**, 220601 (2015).

[58] E. Mascarenhas, H. Flayac, and V. Savona, Matrix-product-operator approach to the nonequilibrium steady state of driven-dissipative quantum arrays, Phys. Rev. A **92**, 022116 (2015).

Nonequilibrium Steady-State Transport in Quantum Impurity Models: a Thermofield and Quantum Quench Approach using Matrix Product States

Supplementary Material

F. Schwarz,[1] I. Weymann,[2] J. von Delft,[1] and A. Weichselbaum[1,3]

[1] *Physics Department, Arnold Sommerfeld Center for Theoretical Physics, and Center for NanoScience, Ludwig-Maximilians-Universität, Theresienstraße 37, 80333 München, Germany*
[2] *Faculty of Physics, Adam Mickiewicz University, Umultowska 85, 61-614 Poznań, Poland*
[3] *Department of Condensed Matter Physics and Materials Science, Brookhaven National Laboratory, Upton, New York 11973-5000, USA*

This supplementary material goes into the details of the numerical calculations. In section S-1 we describe the thermofield in more detail. In section S-2 we describe the discretization we use for the leads. In section S-3 we give some technical details for the MPS implementation. Section S-4 discusses how to determine expectation values, and section S-5 uses an example to illustrate the accuracy of our approach. Section S-6 compares our results for the SIAM at high voltages to previous results, and section S-7 addresses the question of determining the magnetic field at which the Kondo resonance begins to split.

S-1. THE THERMOFIELD APPROACH

The thermofield approach [32–35] used in the main text is a convenient way to represent a thermal state as a pure quantum state in an enlarged Hilbert space with the useful property that this pure state can be expressed as a simple product state. Here, we summarize the analytic details of this approach. For a schematic depiction of its main steps, see Fig. S1.

The density matrix of a thermal state is given by

$$\rho = \frac{1}{Z(\beta)} e^{-\beta H} = \sum_n \underbrace{\frac{e^{-\beta E_n}}{Z(\beta)}}_{\equiv \rho_n} |n\rangle \langle n| \qquad \text{(S1)}$$

with $\beta = 1/T$, $Z(\beta) = \mathrm{tr}\left(e^{-\beta H}\right)$, and $H|n\rangle = E_n|n\rangle$.

Akin to purification [29], one can represent this thermal state as pure state $|\Omega\rangle$ in an enlarged Hilbert space: one doubles the Hilbert space by introducing the auxiliary state space $\{|n_2\rangle\}$, which is a copy of the original Hilbert space $\{|n\rangle\} \equiv \{|n_1\rangle\}$ and defines,

$$|\Omega\rangle = \sum_{n_1,n_2} f_{n_1,n_2}(\beta) |n_1\rangle \otimes |n_2\rangle \qquad \text{(S2)}$$

such that the density matrix ρ can be recovered as

$$\rho = \mathrm{Tr}_{\mathrm{aux}}\left(|\Omega\rangle\langle\Omega|\right) = \sum_{n_2} \langle n_2|\Omega\rangle \langle\Omega|n_2\rangle$$

$$= \sum_{m_1,n_1} \underbrace{\sum_{n_2} f^*_{m_1 n_2}(\beta) f_{n_1 n_2}(\beta)}_{\equiv \rho_{n_1,m_1}} |n_1\rangle \langle m_1| . \qquad \text{(S3)}$$

Thermal equilibrium requires

$$\rho_{n_1,m_1} = \frac{e^{-\beta E_{n_1}}}{Z(\beta)} \delta_{m_1 n_1} . \qquad \text{(S4)}$$

Eq. (S3) implies that the thermal expectation value of any operator A is given by

$$\langle A \rangle_\beta = \langle\Omega|A|\Omega\rangle . \qquad \text{(S5)}$$

For noninteracting systems we can look at each single fermionic mode q separately with Hamiltonian $H_q = \varepsilon_q c_q^\dagger c_q$. The orthonormal basis of our enlarged Hilbert space with modes $c_{q1} = c_q$ and c_{q2} is given by:

$$\left\{ |0,0\rangle_q, |0,1\rangle_q, |1,0\rangle_q, |1,1\rangle_q \right\} . \qquad \text{(S6)}$$

It follows from Eq. (S4) that the cumulative weight of the first two states (where the physical mode is empty) is $(1 - f_q)$ with $f_q = (1 + e^{\beta(\varepsilon_q - \mu_\alpha)})^{-1}$, while the weight of the other two (where the mode is filled) is f_q.

Within the space of the four states in (S6) one can perform a rotation such that one of the new basis states carries the full weight in the thermal state, while the other three do not contribute. This can be exploited to represent $|\Omega\rangle$ as a simple product state. By choosing $f_{00}^{(q)} = f_{11}^{(q)} = 0$ (implying $f_{01}^{(q)}(\beta) = \sqrt{1 - f_q}$ and $f_{10}^{(q)}(\beta) = \sqrt{f_q}$) and rotating such that $|\Omega\rangle = \prod_q |\tilde{0}, \tilde{1}\rangle_q$, we can ensure that this rotation preserves particle number conservation.

The rotated modes are of the form

$$\begin{pmatrix} \tilde{c}_{q1} \\ \tilde{c}_{q2} \end{pmatrix} = \begin{pmatrix} \cos\theta_q & -\sin\theta_q \\ \sin\theta_q & \cos\theta_q \end{pmatrix} \begin{pmatrix} c_{q1} \\ c_{q2} \end{pmatrix} \qquad \text{(S7)}$$

where the angle θ_q is defined by

$$\begin{aligned} \sin\theta_q &= f_{10}^{(q)} = \sqrt{f_q}, \\ \cos\theta_q &= f_{01}^{(q)} = \sqrt{1 - f_q}. \end{aligned} \qquad \text{(S8)}$$

By construction, we then have

$$|\Omega\rangle = \prod_q \underbrace{\left(\sqrt{1 - f_q} |0,1\rangle_q + \sqrt{f_q} |1,0\rangle_q \right)}_{=: |\tilde{0},\tilde{1}\rangle_q} \qquad \text{(S9)}$$

and therefore

$$\tilde{c}_{q1}\,|\Omega\rangle = \tilde{c}_{q2}^\dagger\,|\Omega\rangle = 0\,. \qquad \text{(S10)}$$

Let us conclude with a few further remarks: In the literature [34, 35], one typically transforms to a basis in which $|\Omega\rangle$ is the vacuum of the enlarged Hilbert space.
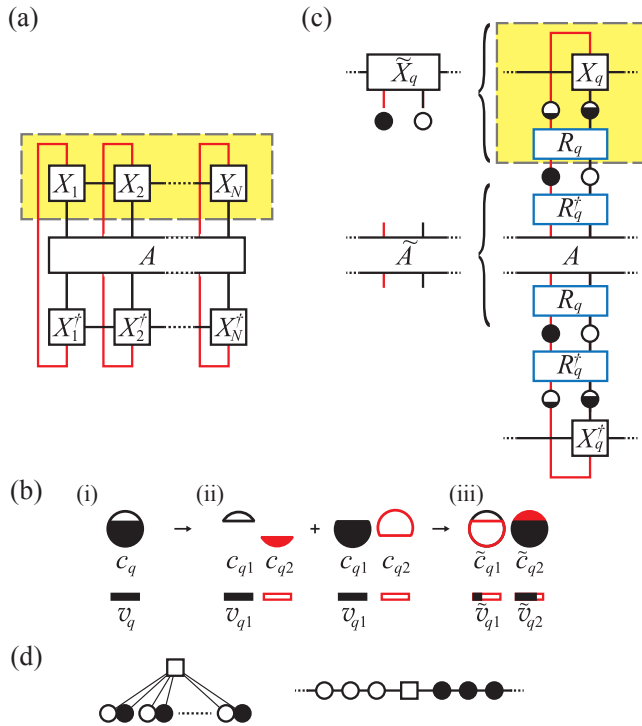

Figure S1.   (a) Schematic MPS representation of the expectation value $\langle A\rangle = \text{tr}(\rho A)$ rewritten in the form $\langle\Omega|A|\Omega\rangle$, where the state $|\Omega\rangle$ with its physical and auxiliary local modes is indicated by the dashed box. (b) Starting from (i) a thermal level occupied with probability f_q we represent the state (ii) as a linear combination $|\Omega\rangle$ of states in which the physical mode is empty or filled, weighting the two contributions corresponding to the Fermi function. We choose the auxiliary mode to be filled (empty) when the physical mode is empty (filled) [see Eq. (S9)]. (iii) The rotation R_q in Eq. (S7), combining the physical mode c_{q1} and the auxiliary mode c_{q2}, yields modes that are empty or filled with probability one, but their coupling to the impurity $\tilde{v}_{qi}$ depends on f_q. (c) Schematic depiction of the thermofield basis transformation for a single fermionic level q. Operators $\tilde{A}$ act on the state $|\Omega\rangle$ represented in the new rotated basis consisting of "holes" and "particles" in terms of the tensors $\tilde{X}_q$. (d) Both purification and local level rotation are set up in the star geometry, where each "free" lead mode couples to the impurity only. We then go over to the chain geometry by tridiagonalizing the modes $\tilde{c}_{qi}$ such that the resulting Hamiltonian consists of nearest-neighbor terms only. We do this for the holes $\tilde{c}_{q1}$ and the particles $\tilde{c}_{q2}$ separately. Since both channels are product states of either completely filled or completely empty levels, a unitary one-particle basis transformation, as provided by the tridiagonalization performed separately within each channel only, necessarily preserves this structure.

This corresponds to the approach presented here, but with the role of $\tilde{c}_{q2}$ and $\tilde{c}_{q2}^\dagger$ interchanged. In this case, the rotation in Eq. (S7) takes the standard form of a Bogoliubov transformation. Using this basis, it would not be necessary to keep the rotated modes in separate channels when going over to an MPS chain. However, the mapping onto a single chain (i) does not eliminate any degrees of freedom, and (ii) comes at the price of loosing particle number conservation. Therefore, for the sake of numerical efficiency, we preferred to keep the two channels separate. The only drawback of the latter approach appears to be that particle and hole excitations are locally separated along the chain geometry which, eventually, may make the accurate description of the long-time behavior more challenging.

The thermofield approach is closely related to the purification approach often used in MPS studies of finite-temperature systems. In particular, both approaches involve doubling the degrees of freedom, introducing an auxiliary mode for each physical mode. But while the latter typically describes interacting systems, the thermofield approach corresponds to its application to noninteracting thermal leads. In many applications of purification, the formulation is chosen such that auxiliary and physical modes are in the same state for the maximally entangled state at infinite temperature. For the thermal state of noninteracting leads at finite temperature, this would correspond to a choice of diagonal $f_{mn}^{(q)}$ in our statement below Eq. (S6), such that

$$|\tilde{\Psi}\rangle = \sqrt{\rho_0}|0,0\rangle + \sqrt{\rho_1}|1,1\rangle \qquad \text{(S11a)}$$

for each single-particle lead level. In comparison to that, we exploit the freedom of unitary transformations in the auxiliary state space and use a number eigenstate instead,

$$|\Psi\rangle = \sqrt{\rho_0}|0,1\rangle + \sqrt{\rho_1}|1,0\rangle\,. \qquad \text{(S11b)}$$

Evidently, Eq. (S11b) can be mapped onto Eq. (S11a) by a particle-hole transformation for the auxiliary degrees of freedom. (In an MPS diagram such as Fig. S1(c), this would amount to flipping the direction of the arrow of all lines [40] representing auxiliary degrees of freedom.) Since such a particle-hole transformation would map our H_aux onto $-H_\text{aux}$, the scheme used here is reminiscent of the purification scheme employed in [47], who used opposite signs for the physical and auxiliary mode Hamiltonians in order to improve numerical efficiency.

Note also that in the present work we purify the thermal leads and do not have an auxiliary degree of freedom for the impurity itself. The reason for this is simple: in the initial state we want to enforce a specific thermal distribution on the occupation statistics of the leads. This carries over to a specific connection between the auxiliary and the physical degrees of freedom in the leads. In contrast, the impurity can be in any state at the beginning of our quench. In particular, one can choose the initial state of the impurity such that the auxiliary mode

for the impurity simply decouples. Also the Hamiltonian dynamics does not connect the auxiliary mode to the rest of the system, so we do not need to describe the auxiliary degree of freedom for the impurity at any time.

Finally, we note that the present scheme of simulating a thermal yet closed system can be extended to open systems. In a previous work [55] we had also introduced a lead representation in terms of "holes" and "particles", yet formulated a description of nonequilibrium steady-state transport through a localized level using Lindblad-driven discretized leads. There we demonstrated, that such a Lindblad driving in effect broadens the discrete levels of discretized leads in such a way that they faithfully mimic the properties of continuous leads. In the basis of "holes" and "particles" this Lindblad driving takes a remarkably simple form and, in particular, it is *local* on the chain underlying the MPS. By adding such a Lindblad driving to the time evolution, it should be possible to describe even longer time scales. However, the price one would have to pay, is a time evolution that is not described by Hamiltonian dynamics but by a Lindblad equation.

S-2. LOG-LINEAR DISCRETIZATION

We want to coarse-grain, i.e. discretize the full band of bandwidth $[-D, D]$ into N energy intervals $[E_n, E_{n+1}]$ in such a way that the width of the energy intervals scales linearly within the transport window (TW) $[-D^*, D^*]$ and logarithmically for energies outside, with a sufficiently smooth transition between the linear sector (lin-sector) and the logarithmic sector (log-sector). Related ideas have been considered in [25, 45]. The three relevant parameters for our discretization are: (i) the level-spacing δ within the lin-sector; (ii) the parameter $\Lambda > 1$ defining the logarithmic discretization in the log-sector (typically $\Lambda \gtrsim 2$; see below); and (iii) the energy scale D^* at which the transition between the lin-sector and the log-sector takes place. To construct such a log-linear discretization we define a continuous function $\mathcal{E}(x)$ which is evaluated at the points $x_n = n + z$ with $n \in \mathbb{Z}$ and $z \in [0, 1)$ to obtain the energies $E_n = \mathcal{E}(x_n)$. This function $\mathcal{E}(x)$ has to fulfill $\mathcal{E}(x + 1) - \mathcal{E}(x) = \delta$ for $|\mathcal{E}(x + 1)| < D^*$ and $\frac{\mathcal{E}(x+1)}{\mathcal{E}(x)} = \Lambda$ $\left(\frac{\mathcal{E}(x)}{\mathcal{E}(x+1)} = \Lambda\right)$ for $\mathcal{E}(x) \gg D^*$ $(\mathcal{E}(x) \ll -D^*)$, respectively. Furthermore, we demand the function and its first derivative to be continuous. We construct such a function by inserting a linear section into the logarithmic discretization described by the sinh() function,

$$\mathcal{E}(x) = \begin{cases} \delta \cdot x & \text{if } |x| \leq x^* \\ \delta \cdot \left(\frac{\sinh[(x \mp x^*)\log \Lambda]}{\log(\Lambda)} \pm x^*\right) & \text{if } x \gtrless \pm x^* \end{cases} \quad \text{(S12)}$$

with $x^* = D^*/\delta$. Fixing the three parameters δ, Λ and D^* fully fixes the form of the function $\mathcal{E}(x)$. The only free parameter left is the parameter $z \in [0, 1)$, whose role is fully analogous to the z-shift in NRG calculations [38, 39].

The outermost intervals are limited by the bandwidth $E_1 = -D$, $E_{N+1} = D$. If one of these outermost intervals gets narrow compared to the adjoining interval, one can simply join these two intervals into one for the sake of energy scale separation within NRG.

The discretization is therefore determined by four parameters: Λ, D^*, δ, and z. The parameter Λ characterizes the logarithmic discretization for the log-sector. It has to be small enough to capture the relevant high-energy physics, but large enough to ensure energy scale separation in the NRG calculation. For our calculations, we typically choose $2 \lesssim \Lambda \lesssim 3$. D^* is the energy scale that defines the size of the TW. If $T \lesssim V$, it is approximately set by the chemical potential $V/2$. If $T \gtrsim V$, temperature will define the size of the TW and the edges of the window will be smeared out. We chose D^* as the energy at which the Fermi function of the channel with positive chemical potential $(\mu = V/2)$ has decreased to a value of 10^{-3}, implying $D^* = V/2$ for $T = 0$ and $D^* \approx 7T$ for $V \ll T$. The level spacing δ in the lin-sector sets the time-scale accessible by the quench calculations before finite size effects get visible. Typically, we set $\delta = D^*/20$, such that we have approximately forty energy intervals within the TW. In all our calculations, we used $z = 0$.

To each of the intervals $[E_n, E_{n+1}]$ we assign an energy ε_n representing the energy of the interval. In the context of NRG, different methods have been developed to optimize this energy [38, 39]. Motivated by Eq. (44) in Ref. [38], we choose a simplified version, namely

$$\varepsilon_n = \begin{cases} \frac{E_{n+1} - E_n}{\ln(E_{n+1}/E_n)}, & \text{if } |E_n|, |E_{n+1}| > D^* \\ \frac{1}{2}\left(E_n + E_{n+1}\right), & \text{else.} \end{cases} \quad \text{(S13)}$$

When $|E_n|$ approaches $|D^*|$ from above, our log-linear discretization approaches a linear discretization, with $E_{n+1} - E_n = \delta$. In this case,

$$\varepsilon_n = \frac{\delta}{\ln(1 + \frac{\delta}{E_n})} \overset{\delta \ll E_n}{\approx} E_n + \frac{\delta}{2} \approx \frac{1}{2}\left(E_n + E_{n+1}\right), \quad \text{(S14)}$$

which matches the definition of ε_n for $|E_n|, |E_{n+1}| < D^*$ in Eq. (S13). In this sense the smooth behavior of the energies E_n defining the discretization intervals leads to a reasonably smooth transition from the log-sector to the lin-sector also in the energies ε_n.

S-3. DETAILS ON THE MPS CALCULATION

All our MPS calculations were built on top of the QSpace tensor library that can exploit abelian as well as non-abelian symmetries on a generic footing [40]. For the SIAM, standard particle-hole symmetry is defined by the spinor $\hat{\psi}^\dagger \equiv (c_\uparrow^\dagger, s c_\downarrow)$, which interchanges holes and particles (up to a sign s) while simultaneously also reverting spin $\sigma \in \{\uparrow, \downarrow\}$ [40]. This symmetry acts independently of the SU(2) spin symmetry, and hence is preserved even if $B \neq 0$. In our simulations, however, we

only exploit U(1) spin and U(1) particle-hole symmetry, since (i) we are also interested in finite magnetic field B, which breaks spin SU(2) symmetry, and (ii) finite bias voltage V breaks particle-hole symmetry in the leads.

A. The MPS geometry

The starting point is the star geometry with the two leads, $\alpha \in \{L, R\}$, discretized in energy with lead levels $q = \{\alpha, (\sigma), k\}$, as depicted in Fig. S2(a). Note that we do not include the chemical potential into the energies ε_q. Together with left/right symmetry for the leads, this implies $\varepsilon_{\alpha(\sigma)k} = \varepsilon_k$. In the thermofield approach the lead levels q are doubled and rotated to "holes" and "particles", represented by the operators $\tilde{c}_{qi}$, as depicted in Fig. S2(b).

a. Decoupling modes: For the positive (negative) high energies in the log-sector the "particle" modes $\tilde{c}_{q2}$ (the "hole" modes $\tilde{c}_{q1}$) are already decoupled due to $f_q = 0$ ($f_q = 1$) without any further rotation. Hence the doubling of levels is not required there.

Furthermore, in the SIAM, we can combine the "holes" and "particles" separately from the left lead with those from the right lead into new modes,

$$\tilde{C}_{k\sigma i} = \frac{1}{\mathcal{N}} \sum_\alpha \tilde{v}_{\alpha k\sigma i} \tilde{c}_{\alpha k\sigma i} \ , \quad \left(\mathcal{N}^2 \equiv \sum_{\alpha'} |v_{\alpha' k\sigma i}|^2\right) \tag{S15a}$$

yielding the geometry in Fig. S2(c). The modes orthogonal to these,

$$\tilde{C}_{k\sigma i}^{(\perp)} = \frac{1}{\mathcal{N}} \left(\tilde{v}_{Lk\sigma i}^* \tilde{c}_{Rk\sigma i} - \tilde{v}_{Rk\sigma i}^* \tilde{c}_{Lk\sigma i}\right) , \tag{S15b}$$

decouple from the impurity. In matrix notation, temporarily suppressing the global index set $k\sigma i$ for readability, this can be written as

$$\begin{pmatrix} \tilde{C} \\ \tilde{C}^{(\perp)} \end{pmatrix} = \frac{1}{\mathcal{N}} \begin{pmatrix} \tilde{v}_L & \tilde{v}_R \\ -\tilde{v}_R^* & \tilde{v}_L^* \end{pmatrix} \begin{pmatrix} \tilde{c}_L \\ \tilde{c}_R \end{pmatrix} \tag{S16a}$$

with inverse relations,

$$\begin{pmatrix} \tilde{c}_L \\ \tilde{c}_R \end{pmatrix} = \frac{1}{\mathcal{N}} \begin{pmatrix} \tilde{v}_L^* & -\tilde{v}_R \\ \tilde{v}_R^* & \tilde{v}_L \end{pmatrix} \begin{pmatrix} \tilde{C} \\ \tilde{C}^{(\perp)} \end{pmatrix} \tag{S16b}$$

The decoupling of the orthogonal modes is in complete analogy to standard equilibrium calculations in the SIAM [24]. In our setup it carries over to the nonequilibrium situation, because the difference in the chemical potential of the two physical leads is shifted into the couplings $\tilde{v}_{qi}$. In the IRLM, this combination of left and right lead modes is not possible, because the two leads couple to two different impurity sites, in full analogy to standard equilibrium calculations.

The above analysis leads to the remarkable conclusion that the numerical effort for the description of the spinless IRLM is comparable to that of the spinful SIAM.
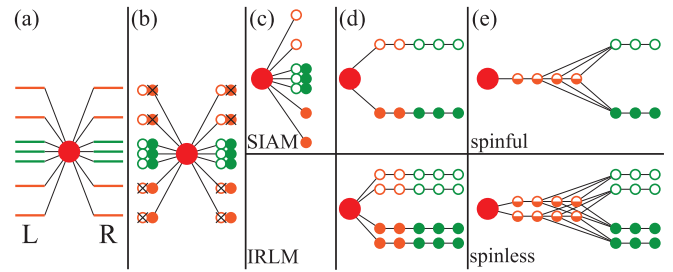

Figure S2. Sketch of the different discrete site geometries. (a) We start with two channels $\alpha \in \{L, R\}$ in the star geometry, with the two colors representing the log-sector and the lin-sector. (b) Within the thermofield approach each level is exactly represented by one "hole" and one "particle". However, for the positive (negative) energies in the log-sector the "particles" ("holes") decouple from the impurity due to $f_q = 0$ ($1 - f_q = 0$), respectively. (c) For the SIAM, only specific linear combinations of left and right lead modes couple to the impurity, while the corresponding orthogonal modes decouple see Eqs. (S15) (d) Tridiagonalizing "holes" and "particles" into separate channels, we get two channels in the chain geometry for the SIAM (upper part) and four in the IRLM (lower part), for which we still distinguish between left and right leads. The couplings in the log-sector for each channel decay as Λ^{-n} (e) Recombination of holes and particles within log-sector into one channel using another tridiagonalization since for NRG it is unfavorable to have "holes" and "particles" in separate channels. The couplings in this altered channel setup decay as $\Lambda^{-n/2}$, which resembles equilibrium NRG. However, the first site of the lin-sector in the chain geometry now couples to a range of sites of towards the end of the log-sector. Nevertheless, energy scale separation ensures that this nonlocality is restricted to only a few sites.

The additional cost involved for the SIAM for treating two states is compensated by the simplification that left and right lead modes can be combined because they couple to the same impurity site.

b. Tridiagonalization: When going over to a chain geometry, the corresponding tridiagonalization is performed for "holes" and "particles" independently (treating them as different "channels"), in order to maintain the property that the thermal state $|\Omega\rangle$ is a simple product state while also preserving charge conservation: if for the state $|\Omega\rangle$ a channel is completely empty (filled) in the star geometry, it will remain a completely empty (filled) channel also in the chain geometry. For the IRLM, since the left and right leads have to be represented as separate channels, we tridiagonalize the modes $\tilde{c}_{qi}$ into the four channels $\{\alpha i\}$ with $\alpha \in \{L, R\}$ and $i \in \{1, 2\}$ labeling "holes" and "particles", see lower part of Fig. S2(d). For the SIAM, in contrast, left and right leads are combined in the sense of equation (S15a), so we separately tridiagonalize the "holes" ($\tilde{C}_{q,i=1}$) and the "particles" ($\tilde{C}_{q,i=2}$), see upper part of Fig. S2(d).

Due to energy scale separation, the first part of the chain corresponds to the energy scales of the log-sector, while the later part of the chain represents the lin-sector. Instead of counting the exact number of sites in the chain

geometry, we identify the log-sector by looking at the behavior of the hoppings which decay exponentially in the log-sector and are all of the same order in the lin-sector. Due to the smoothened transition from the linear to the logarithmic discretization also the hopping matrix elements show a smooth crossover from exponential decay to approaching a constant. We define the log-sector on the chain as the part for which (i) the hoppings decay strongly enough (the details of this condition slightly depend on the number of many-particle states kept in the NRG iterations) and (ii) the hoppings are larger than the energy scale D^* on which transport takes place. By construction the two conditions are roughly equivalent. Note that for the "holes" ("particles") in the log-sector of the star geometry only the positive (negative) energies contribute to the hybridization. This translates into a decay of the hoppings and on-site energies scaling as Λ^{-n} for the log-sector on the chain.

c. Re-combining "holes" and "particles" in the log-sector: For the NRG calculation it is disadvantageous to describe "holes" and "particles" in separate channels since particle-hole excitations are sharply separated in terms of the particle and the hole content along the chain geometry. Consequently, we apply a further tridiagonalization that remixes "holes" and "particles" of the log-sector into one channel, e.g. see upper part of Fig. S2(e). This then defines the renormalized impurity (RI). For the IRLM, this subsequent tridiagonalization is done for the left and right lead separately, see lower part of Fig. S2(e). After this recombination the hoppings in the channel(s) will decay as $\Lambda^{-n/2}$. The numerical complexity of the NRG calculation, therefore, is comparable to that of a standard equilibrium calculation in the sense that we obtain the same number of numerical channels (one spinful for the SIAM, two spinless for the IRLM) and the same exponential decay in the energy scales. Note that the tridiagonalization combining "holes" and "particles" for the log-sector comes with the caveat that it introduces a nonlocality in the Hamiltonian: after this further tridiagonalization, the first site in the lin-sector does not only couple to the last site of the log-sector but rather to the last few sites, see Fig. S2(e). The corresponding hopping term is therefore subject to truncation within the NRG iterations. However, energy-scale separation ensures that this nonlocality stretches only over a few sites, so the error introduced by the truncation of this hopping is considered minor.

d. Remaining lin-sector: For the DMRG calculation we order the channels such that the "holes" are on one side of the RI and the "particles" on the other side, see Fig. 1. The local dimension of each chain element is given by $2^2 = 4$: in the SIAM this is due to the spin degree of freedom σ, in the IRLM it represents the remaining degree of freedom in the physical leads α.

In case of the IRLM, where left and right lead are kept separate, there is one further point worth noting: at $T = 0$, also in the lin-sector either the "hole" or the "particle" decouples from the impurity for each lead level

q. This implies that parts of the remaining chains representing "holes" and "particles" in the log-sector of the chain geometry decouple. This fact can be applied to further reduce the numerical cost, even though we have not done so here. It stems from the fact that no purification procedure is needed for $T = 0$, and therefore does not carry over to $T > 0$.

B. Renormalized Impurity

The log-sector traces out the high-energy degrees of freedom at energies $E \gg T, V$. Therefore the renormalized impurity represents the low-energy many body basis that still spans energies up to and beyond the transport window (TW) set by $\max(T, V)$. Typically we keep approximately 500 to 700 states to describe this basis. In the quench protocol, we can pick an arbitrary pure state $|\phi_{\text{ini}}\rangle$ in this effective low-energy space as the initial state for the RI. In order to avoid excess energy in the initial state, we choose the ground state of the log-sector.

If the ground state space is degenerate by symmetry, picking a single individual state may artificially break that symmetry. Therefore proper averaging over degenerate state spaces is required, either by actually running separate simulations for each degenerate ground state, or by simply exploiting the known effect of the symmetry on the numerical result. (This also applies to the case of quasi-degenerate ground states, e.g. when a symmetry present in the Hamiltonian is only weakly broken.) Overall, note that degeneracy within the log-sector is rather generic, since we choose to keep particle and hole channels symmetric. Therefore we combine the *same* number of "hole" and "particle" sites into the log-sector such that, including the impurity site, it always contains an odd number of sites [see Fig. S2].

For example, for the IRLM at particle-hole symmetry, the log-sector has a single zero-energy level, $\varepsilon_c = 0$, causing the ground state sector to be two-fold degenerate. Since our NRG code exploits abelian particle number conservation, we obtain two ground states for the log-sector that are particle-number eigenstates globally within the RI, say $|G_1\rangle$ and $|G_2\rangle$. We can initialize our quench calculations by taking $|\phi_{\text{ini}}\rangle$ equal to either $|G_1\rangle$ or $|G_2\rangle$.

Now, for a particle-hole-symmetric model involving a zero-energy level coupled to an *infinite* bath, the local (e.g. thermal) occupancy is $n_C = 1/2$. However, the initial local occupancies for the two number eigenstates above, say $n_{C,i} = \langle G_i|\hat{n}_C|G_i\rangle$ (for $i = 1, 2$), are not necessarily equal. In general, $n_{C,1} + n_{C,2} = 1$, yet $n_{C,1} \neq n_{C,2}$ due to finite-size effects (the log-sector involves only a *finite* number of bath levels). Correspondingly, during the post-quench time evolution, only the average of the local occupancies, $\langle n_C\rangle(t) \equiv \frac{1}{2}(n_{C,1} + n_{C,2})(t) = 1/2$, throughout, whereas the local occupancies for the two individual states, $n_{C,i}(t)$, reach the value $1/2$ only in the asymptotic limit $t \to \infty$ due to their hybridization with

the lin-sector. In practice, by knowing the underlying symmetry which enforces $n_{C,2}(t) = 1 - n_{C,1}(t)$, the inialization of the quench may only include e.g. $|G_1\rangle$, bearing in mind that the data must be symmetrized w.r.t. occupation.

Alternatively, one could construct linear combinations of $|G_{1,2}\rangle$, say $|G_\pm\rangle$, which are eigenstates of a particle-hole transformation with eigenvalues ± 1, and which yield local occupancies, $n_{C,\pm} = \langle G_\pm | \hat{n}_C | G_\pm \rangle$, that by construction satisfy $n_{c,\pm} = 1/2$. If we would initialize the quench by taking $|\phi_{\rm ini}\rangle$ equal to either $|G_+\rangle$ or $|G_-\rangle$, then we would find $n_{C,\pm}(t) = 1/2$ throughout the post-quench time evolution. However, since the post-quench time evolution conserves particle number within each particle-number eigensector, this strategy would be equivalent to averaging the result of two separate quenches, initialized with $|\phi_{\rm ini}\rangle$ equal to $|G_1\rangle$ or $|G_2\rangle$, respectively.

C. Trotter time evolution

The initial state is evolved in time, $|\Psi(t)\rangle = e^{-iHt} |\Psi(t=0)\rangle$, using tDMRG [27–29] with a standard second-order Trotter decomposition for a time step τ:

$$e^{-iH\tau} = e^{-iH_o\tau/2} e^{-iH_e\tau} e^{-iH_o\tau/2} + \mathcal{O}(\tau^3), \qquad \text{(S17)}$$

where H_e (H_o) includes all "even" ("odd") bonds. The individual terms in Eq. (S17) w.r.t. H_e (H_o) will be referred to as even (odd) Trotter steps or even (odd) iterations, respectively. The tensorial operations that are performed in practice within the MPS setup, are sketched in Fig. S3. The RI is described within a fixed effective low-energy basis. The main idea is to use this fixed basis as the local state space of an MPS site in the center when performing the Trotter time evolution. However, when constructing the time evolution operator that contains the coupling between the NRG sites and the first of the remaining sites, one has to be careful with the exponentiation of the coupling term. For this purpose, we need to consider two subsequent NRG iterations, e.g. at Wilson chain lengths N and $N + 1$, where site $N + 1$ will be referred to as flexible site. These will be treated differently in the even compared to the odd Trotter steps (depending on the exact chain length, the notion of "even" and "odd" may need to be interchanged). For the time steps which we call "even" in panel (a), we exponentiate the full Hamiltonian of N NRG sites plus the flexible site ($H_{N+1}^{\rm NRG}$), yet excluding the coupling to the rest of the chain. Therefore we *fully* associate the "local" Hamiltonian of the RI with even iterations which is allowed within the Trotter setup. Assuming that the Wilson chain length $N + 1$ is still within the realm of energy scale separation, it can be dealt with in standard NRG manner. In particular, it can be exactly diagonalized in the expanded state space, including the state space of the flexible site, followed by simple exponentiation. The couplings between the flexible site and the subsequent sites, i.e. sites $N + 1$ and $N + 2$, both left and right, we reshape the tensors as depicted in Fig. S3(b). Note that this requires fermionic swap gates [41] to account for the correct treatment of fermionic signs. After this reshaping the performance of the "odd" time steps is standard, as sketched in Fig. S3(c).

At time $t = 0$, the RI is in its ground state, while the leads are thermal. Since we are interested in the nonequilibrium steady-state properties, we do not switch on the coupling between RI and thermal leads abruptly in our quench protocol, as this would introduce undesirable high-energy excitations into the system. Instead, with adiabaticity in mind, we turn on the coupling between RI and thermal leads smoothly over a short time interval. The detailed form of this procedure should not matter. In our calculation, we ramp up the coupling η between the RI and the thermal leads in a linear fashion: we use a time window of $t_{\rm ramp} = 2/D^*$ to $4/D^*$ and divide it into $N = 10$ to 20 equally spaced time intervals with stepwise constant couplings, $\eta(t_n) = \eta \frac{n}{N}$ where $n = 1, \ldots, N$.

The size of the actual Trotter time step τ in equation (S17) should scale with $E_{\rm trunc}^{-1}$, with $E_{\rm trunc}$ being the highest eigenenergy of the truncated NRG basis (or, if no NRG is required, the many-body energy bandwidth, i.e. since all energy scales are only moderately smaller as compared to the bandwidth of the leads). In practice, a prefactor of in the range 0.5 to 1 worked quite well. In our calculation this energy $E_{\rm trunc}$ typically is of the order $5D^*$ to $20D^*$.

When applying the Trotter gates, we keep all singular values larger than some threshold $\varepsilon_{\rm (SVD)}$. Within our calculation this threshold varies between $\varepsilon = 2 \cdot 10^{-4}$ and $\varepsilon = 10^{-3}$. We time-evolve the system until a time $t_{\rm max}$ at which a maximal bond dimension $D_{\rm max}$ is reached in our MPS due to an increase in entanglement entropy following the quench. We used $D_{\rm max}$ up to 450 in our calculations. The above parameters implied typical accessible times in the post-ramp window up to $t_{\rm max} - t_{\rm ramp} > 8/D^*$. In case of $V \gg T$ this is equivalent to $t_{\rm max} > 16/V$. Compared to an oscillation period of $4\pi V^{-1}$ in the current (see below) this range might seem rather small. However, typically these oscillations are (a) strongly reduced in amplitude due to the quasi-adiabatic quench protocol as described above, and (b) in cases where the oscillations are nevertheless still strong, i.e. at large voltages, the accessible time window typically can be extended over many periods.

S-4. EXPECTATION VALUES AND CONVERGENCE

A. Current

For the IRLM, the current through the central site of the impurity can be defined by looking at the change of the corresponding occupation number, $\frac{d}{dt} \langle n_C \rangle$. In the steady state this derivative should be zero, of course, but we can identify the contribution, J_α, of the current flow-
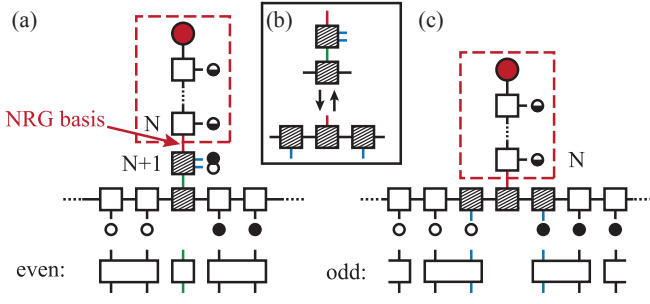
Figure S3. Sketch to illustrate how NRG and DMRG are combined in the Trotter time evolution. (a) For the performance of the "even" time steps we exponentiate the Hamiltonian of all NRG sites plus one additional site in the sense of standard NRG. For the "odd" time steps we rearrange the tensors as depicted in (b) including fermionic swap gates to bring the MPS into a form with local Trotter gates. (c) The time evolution on the "odd" bonds is then a standard tDMRG step. The boxes at the bottom in both, (a) and (c), indicate the Trotter gates to be applied.

ing from lead α into the dot from the formula

$$0 = \frac{d}{dt} e \langle \hat{n}_C \rangle = \sum_{\alpha} \underbrace{\frac{2e}{\hbar} \mathrm{Im}\big(t' \, \langle d_C^\dagger d_\alpha \rangle\big)}_{\equiv J_\alpha}. \qquad (S18)$$

In the SIAM we combine the modes of the left and right channels as given in Eqs. (S15). Still, it is possible to deduce the current from the change of occupation $\frac{d}{dt} \langle \hat{n}_{d\sigma} \rangle$ at the central site:

$$J_{\alpha\sigma} = \frac{2e}{\hbar} \sum_k \mathrm{Im}\big(v_q \langle d_\sigma^\dagger c_q \rangle\big) = \frac{2e}{\hbar} \sum_{ki} \mathrm{Im}\big(\tilde{v}_{qi} \langle d_\sigma^\dagger \tilde{c}_{qi} \rangle\big)$$

$$= \frac{2e}{\hbar} \sum_{ki} \frac{|\tilde{v}_{qi}|^2}{\sqrt{\sum_{\alpha'} \tilde{v}_{\alpha' k\sigma i}^2}} \mathrm{Im}\big(\langle d_\sigma^\dagger \tilde{C}_{k\sigma i} \rangle\big). \qquad (S19)$$

where we used Eq. (S16b), $\tilde{c}_{\alpha k\sigma i} = \frac{\tilde{v}_{\alpha k\sigma i}^*}{\mathcal{N}} \tilde{C}_{k\sigma i} + ... \tilde{C}_{k\sigma i}^{(\perp)}$, together with the fact that the mode $\tilde{C}_{k\sigma i}^{(\perp)}$ decouples from the impurity and therefore $\langle d_\sigma^\dagger \tilde{C}_{k\sigma i}^{(\perp)} \rangle = 0$. The chain operators underlying the MPS $f_{n\sigma(i)}$ are related to the modes $\tilde{C}_{k\sigma i}$ by a unitary transformation, which includes the mapping of "holes" and "particles" onto a chain and the re-combination of channels within the RI. The expectation values $\langle d_\sigma^\dagger \tilde{C}_{k\sigma i} \rangle$ can therefore be determined by calculating the expectation values $\langle d^\dagger f_{n\sigma(i)} \rangle$ for all chain sites n. For the SIAM, the current can further be divided into different spin contributions $J_{\alpha\sigma}$.

Interestingly, in most cases the *symmetrized* current

$$J_{(\sigma)} = \frac{1}{2} \big(J_{L(\sigma)} - J_{R(\sigma)}\big). \qquad (S20)$$

converges much faster than $J_{L(\sigma)}$ and $J_{R(\sigma)}$ separately [see discussion of Fig. S4(h) below for details]. For the SIAM, a similar statement holds when averaging over spin instead of averaging over channels. In practice, we take the mean over both by defining

$$J = (J_\uparrow + J_\downarrow) = \frac{1}{2} \big(J_{L\uparrow} - J_{R\uparrow} + J_{L\downarrow} - J_{R\downarrow}\big) \qquad (S21)$$

We define the value of the steady-state current $J(V)$ by taking the mean over the last part of $J_V(t)$, where the current is converged to its steady-state value. If the oscillations are pronounced, we take the mean over a time window, which equals an integer number of periods, in many cases simply the last period. The conductance is obtained from

$$g(V^*) = \frac{J(V_1) - J(V_2)}{V_1 - V_2} \left(\frac{2e^2}{h}\right)^{-1} \qquad (S22)$$

with $V^* = \frac{1}{2}(V_1 + V_2)$, and V_1 and V_2 close to each other, where we average $J_{V_1}(t)$ and $J_{V_2}(t)$ over similar time windows.

B. Dot Occupation

The occupation of the impurity in the SIAM, as well as the occupation of the central site of the impurity for the IRLM are of physical relevance. Their time evolution is related to that of the current via

$$\frac{d}{dt} e \langle n_{C/d}(t) \rangle = J_L(t) + J_R(t) \qquad (S23)$$

In the present work, we focus on the particle-hole symmetric point. Because of this symmetry we expect the steady-state value of $n_{C/d}$ to be independent of voltage and given by $n_C = \frac{1}{2}$ in the IRLM and $n_d = n_{d\uparrow} + n_{d\downarrow} = 1$ in the SIAM. The magnetization $M = \frac{1}{2}(n_{d\uparrow} - n_{d\downarrow})$, however, is a nontrivial function of voltage and magnetic field.

C. Long-time convergence after the quench

By definition, in the nonequilibriuim steady state (NESS) all expectation values are converged in the sense that they do not change with time. However, we are limited to a finite time window and cannot fully reach this point. In this section, we discuss this aspect in more detail based on the behavior of the symmetrized current J, the currents from the left and right leads $J_{\alpha(\sigma)}$, and the (spin-resolved) dot occupation n_C or $n_{d(\sigma)}$.

As explained above, our initial state breaks certain symmetries. However, as we assume the steady state to be unambiguous, we expect it to obey the symmetries of the Hamiltonian.

For the IRLM we have done our calculations at the particle-hole symmetric point. We therefore expect $n_C = 1/2$ in the steady state. And, if the dot occupation is converged, one finds $J_L = -J_R$ because of Eq. (S23). This is, indeed, what we find for low voltages, see Fig. S4(b). For higher voltages, however, we do not see full convergence in n_C, see Fig. S4(d). Consequently, also the currents are not converged, so we do not find $J_L = -J_R$. However, the *symmetrized* current J is converged, except for oscillations around a well-defined mean value. These oscillations do have the expected period of $\frac{4\pi}{V}$ [42], and
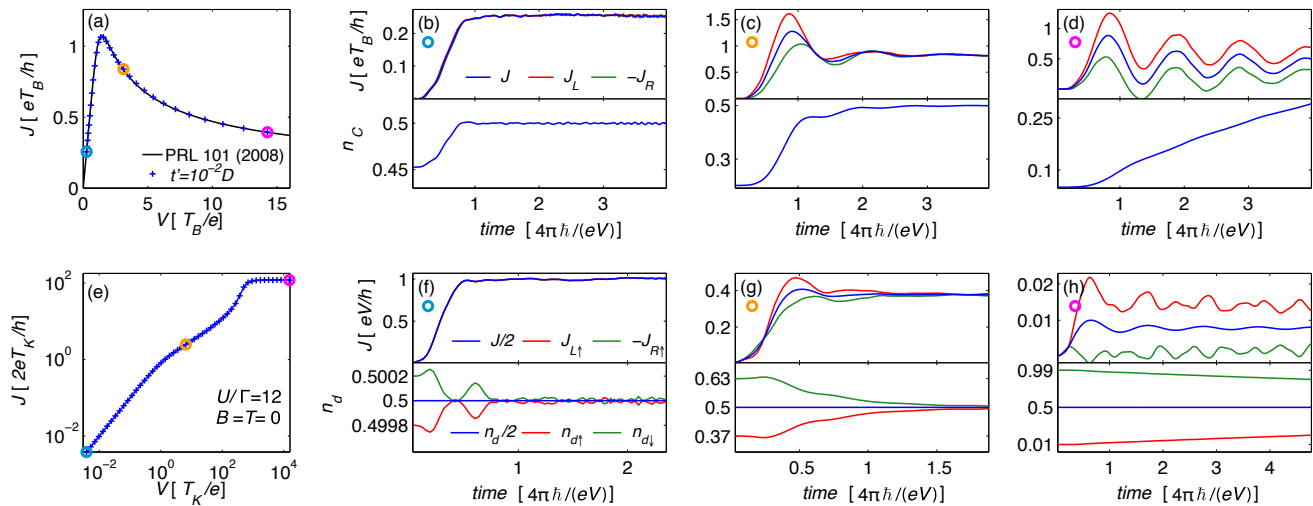
Figure S4. Upper panels: convergence in the IRLM — Panel (a) replots the data set for $t' = 10^{-2}D$ in Fig. 2 of the main text. Panels (b-d) show the time dependence of the currents J_L, $-J_R$ and $J = (J_L - J_R)/2$ and the dot occupation n_C, for the three different voltage values marked by circles in panel (a), respectively. For the lowest voltage which is still in the linear response regime, we find nice convergence in the dot occupation and the current (panel b). With increasing voltage, all three currents develop increasingly strong oscillations, with a period of $4\pi/V$, as expected (panels c,d). For the largest voltage we do not find convergence in n_C (panel d). This reflects in the fact that also J_L and J_R are not yet converged. However, the symmetrized current J (blue line) does oscillate around a well-defined mean value. Lower panels: convergence in the SIAM — Panel (e) replots the data for $U = 12\Gamma$ and $T = 0$ in Fig. 3 (a) of the main text. Panels (f-h) show the behavior of $J_{L\uparrow}$ and $J_{R\uparrow}$, J, and $n_{d\sigma}$ (at $T = B = 0$) for the voltage values marked in circles in panel (e), respectively. The current for the down-spin is not shown, since $J_{L\downarrow} \approx -J_{R\uparrow}$ and $J_{R\downarrow} \approx -J_{L\uparrow}$. The total dot occupation n_d is equal to 1 in the beginning and remains so throughout. However, for large voltages the numerically accessible time window is too short to find convergence for the spin-resolved occupations $n_{d\uparrow}$ and $n_{d\downarrow}$. In panel (h), the left and right components of the current (red and green lines) show seemingly irregular oscillations; these arising from a combination of large voltage and the finite level spacing in the lin-sector. The level-spacing effect cancels out, however, for the symmetrized current, $J = (J_L - J_R)/2$ (blue line), which shows regular oscillations with the expected period of $4\pi/V$.

the amplitudes decay rapidly. The initial state breaks particle-hole symmetry as explained above. This symmetry breaking is more pronounced for shorter NRG Wilson chains. This is the reason why for small voltages (for which the TW is small so that the NRG Wilson chain is long) we already start with $n_{d\sigma}(t = 0) \approx \frac{1}{2}$ while for high voltages (for which the TW is large and the NRG Wilson chain is short) the symmetry breaking in the beginning is very strong.

Analogous considerations apply for the SIAM. We numerically observe the behaviour

$$J_{L\sigma}(z) \approx -J_{R,-\sigma}(t) \qquad (S24)$$

and $n_d(t) = n_{d\uparrow}(t) + n_{d\downarrow}(t) \approx 1$ for all times t, reflecting particle-hole and left-right symmetry (here $-\sigma$ stands for reverted spin σ). However, by choosing a specific initial pre-quench state out of a degenerate ground state multiplet, this breaks the spin symmetry, and hence we find $n_{d\uparrow}(t) \neq n_{d\downarrow}(t)$, even for $B = 0$. The effect of this symmetry breaking is largest for high voltages. Whereas for small voltages we do find convergence in the dot occupation [e.g. see Fig. S4(f)], for high voltages our numerically accessible time window is too small to see convergence [Fig. S4(h)]. Moreover, for large voltages the

spin-resolved currents $J_{L\sigma}$ and $J_{R\sigma}$ show seemingly irregular oscillations, as seen in Fig. S4(h). A Fourier-transform analysis (not shown) reveals that the oscillations in $J_{\alpha\sigma}(t)$ have several characteristic frequencies, one being $\frac{V}{4\pi}$ (as expected from [43]), the others being the energies representing the intervals in the log-sector closest to D^*, which was chosen $D^* = V/2$ here. Thus, at large voltages the post-quench dynamics become sensitive to the rather crude discretization in the log-sector, causing the seemingly irregular oscillations in the spin-resolved currents at large voltages. This suggests that the strength of these discretization-related oscillations could be reduced, if desired, by using a slower ramp for the quench (i.e. a larger ramping time t_{ramp}), or by reducing the size of the log-sector (i.e. increasing D^*, while keeping the level spacing δ for the lin-sector fixed). In practice, though, we found this to be unnecessary, since the discretization-related oscillations cancel in the left-right symmetrized current: $J = (J_L - J_R)/2$ shows only regular oscillations around a well-defined mean value [Fig. S4(h)] with the expected time-period of $\frac{4\pi}{V}$ [43], similar to those found for the IRLM. We suspect that this cancellation of discretization-related oscillations occurs because our treatment of the leads respects left-
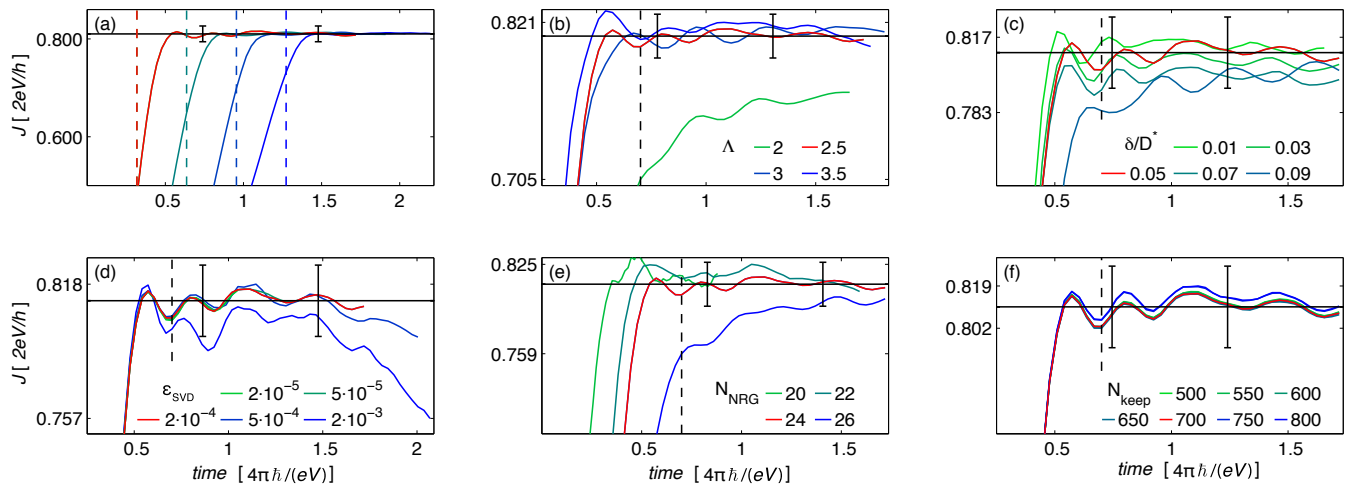
Figure S5. Illustration of the numerical accuracy using the example of $V = T_K$ with the parameters as in Fig. 3(a), with $U/\Gamma = 12$. In each of the panels the red curve corresponds to the parameters typically used for our calculations and the "error bars" indicate a relative range of $\pm 2\%$ around the mean. Panel (a) shows $J(t)$ where the coupling between RI and leads is turned on quasi-adiabatically over time windows of four different widths. All curves approach the same steady-state value. In (b) and (c) the discretization parameters Λ and δ are varied. In (d) different thresholds, ε_{SVD}, are used for the SVD truncation in the tDMRG quench. In (e) the number of sites treated with NRG is changed (and therefore the number of sites treated with tDMRG is changed accordingly). And finally in (f) we use different numbers of kept states in the effective NRG basis for the renormalized impurity.

right symmetry, both regarding their discretization [see Fig. S2(d,e)] and when turning on the coupling between the log- and lin-sectors during the quench.

In the case of finite magnetic field in the SIAM, we do not have spin symmetry. In particular, we expect $n_{d\uparrow} \neq n_{d\downarrow}$, even in the steady state. The exact NESS values of $n_{d\sigma}$ are nontrivial and depend on voltage. However for large values of V, we are not able to see convergence in these occupations, analogously to Fig. S4(h). Still, it is in principle possible to predict the NESS occupation by extrapolating the data available within the accessible time window, e.g. using linear prediction [44].

S-5. NUMERICAL ACCURACY

Our approach treats the many-particle aspect of impurity models nonperturpatively. However, of course, the numerics contains approximations such as the discretization of the lead into a finite number of energy intervals, the truncation of states within the NRG, and the truncation of the MPS within the tDMRG time evolution. A further error arises from the fact that we have to take the mean over a curve $J(t)$ that often still oscillates over a well-converged mean value. Therefore it is difficult to give a precise value for our error. However, we can provide an estimate for the error bar. For the case of the current, it is approximately $\pm 3\%$, throughout, which at times may be considered conservative.

To illustrate this statement we go into more detail for the curve $J(t)$ for the parameters used in Fig. 3(a) with

$U/\Gamma = 12$ at $V \approx T_K$: Fig. S5 shows the behavior of $J(t)$ when varying various different numerical parameters, such as discretization and truncation parameters. In each of the panels the red curve was obtained from the parameter choices typically used in our numerics. This curve is identical in each of the panels. The black horizontal line shows the mean value obtained for times after the vertical dashed black marker. The "error bars", for convenience, indicate a range of $\pm 2\%$ around the mean value. The essential message from all these plots is that even though our results do show slight dependence on the various numerical parameters that were varied here, this dependence is small, and within the stated error bars of $\lesssim 2$ to 3%. Depending on the precise parameters the curves in some cases wiggle more strongly, or for higher voltages show stronger oscillations. In this cases, the error is closer to the upper end of the estimated error range. Looking at the comparison of $U = 0$ with exact results and the comparison of $g(T,0)$ with NRG values in Fig. 3(a), confirms this estimate for our error bar.

S-6. COMPARISON TO OTHER METHODS

In Ref. [6] previous tDMRG quench results on the high-voltage regime of the SIAM are compared to results obtained via the functional renormalization group (FRG) and real-time quantum Monte Carlo (rt-QMC), see Refs. [6, 7] for details on the different methods. Fig. S6 shows the data of Fig. 2 in Ref. [6] together with further rt-QMC results taken from Ref. [7]. For compar-
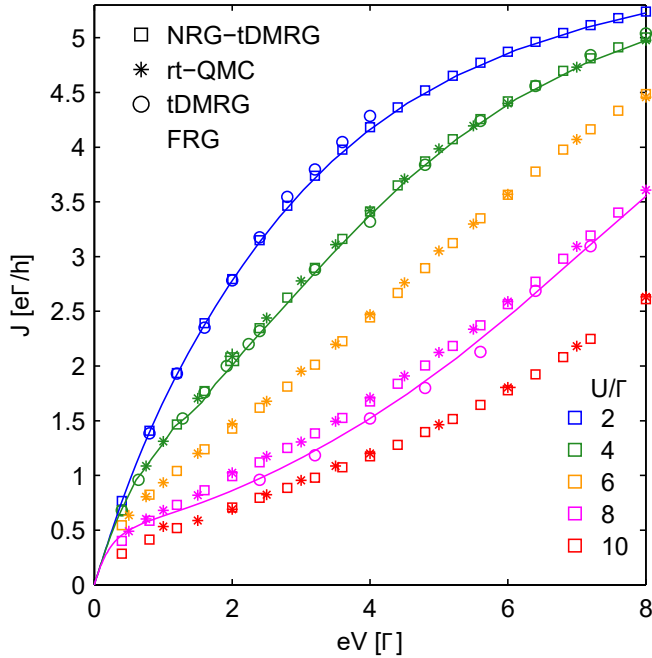
Figure S6. Current in the SIAM as a function of voltage in the high-voltage regime, $V \gtrsim \Gamma$, for different values of U/Γ: we compare results obtained with our method (NRG-tDMRG) to results from rt-QMC, previous tDMRG calculations, and FRG (see Refs. [6, 7] for details). For a range of U/Γ values our results nicely agree with previous results.
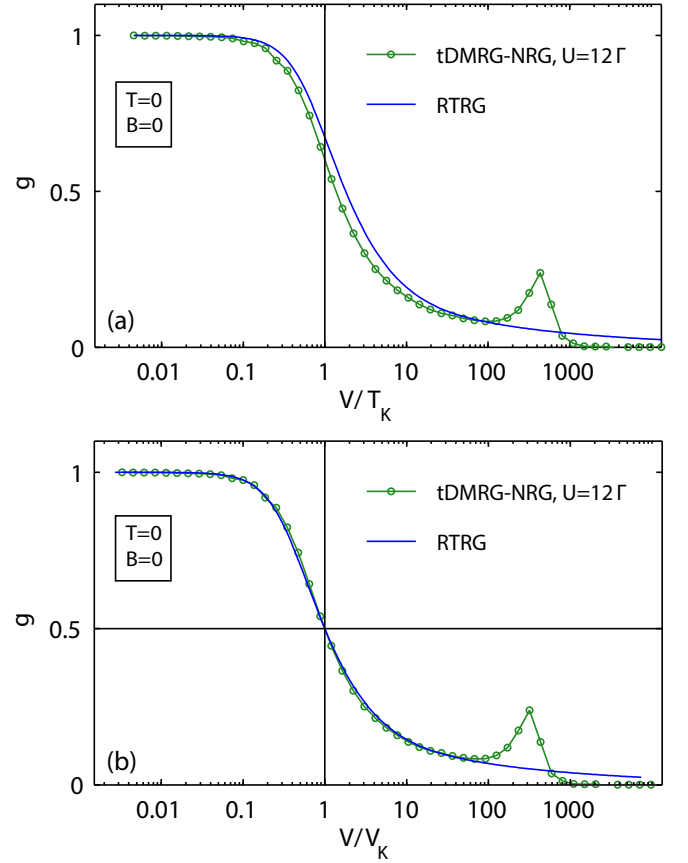

Figure S7. (a) Comparison of $g^{T=0}(V)$ vs. V/T_K on a logarithmic scale, computed at $B = 0$ in the Kondo limit. The data points (circles) show the NRG-tDMRG result for $U/\Gamma = 12$, replotting the corresponding curve from Fig. 3(a) of the main text. The solid curve shows the RTRG results of Pletyukhov and Schoeller [8] for the Kondo model, plotted using Eqs. (S26). The small high-energy peak of the tDMRG-NRG curve reflects charge fluctuations not captured by the Kondo model. (b) Same data, but now plotted vs. V/V_K.

ison, we here also include results obtained in our NRG-tDMRG quench setup. For all parameters our data nicely agree with the rt-QMC data. For $U/\Gamma = 8$, tDMRG and FRG slightly differ from the rt-QMC results (and thus also from our results). This has already been discussed in Ref. [6]. Note, however, that the parameter regimes of these reference systems stayed far away from low-energy Kondo scales since for the larger values of U/Γ the described regime corresponds to $V \gg T_K$, while the small values of U/Γ do not describe the Kondo limit.

We also compare our results for the nonlinear conductance to those obtained by Pletyukhov and Schoeller for the Kondo model using the real-time renormalization group (RTRG) in Ref. [8]. They found that the temperature and voltage scales at which the conductance reaches $\frac{1}{2}$, defined via

$$g^{V=0}(T = T_K) = \frac{1}{2}, \qquad g^{T=0}(V = V_K) = \frac{1}{2}, \quad \text{(S25)}$$

differ, with $V_K/T_K \approx 1.8$. (They use the notation $T_K^* = T_K$ and $T_K^{**} = V_K$.) Their result for the nonlinear conductance can be fit well using the trial function

$$g_{\mathrm{RTRG}}^{T=0}(V) \approx \left\{ 1 + [V/T_K'(x)]^2 \right\}^{-s}, \quad x = V/V_K,$$

$$T_K'(x) = T_K^{**} \left(\frac{1 - b + bx^{s'}}{2^{\frac{1}{s}} - 1} \right)^{\frac{1}{2}}, \quad \text{(S26)}$$

using $s = 0.32$, $b = 0.05$ and $s' = 1.26$. Assuming that our data for $U/\Gamma = 12$ in Fig. 3 of the main text is deep in the Kondo limit, we compare our data for $g^{T=0}(V)$ vs. V/T_K to theirs in Fig. S7(a). Our curve for the nonlinear conductance has a shape similar to theirs, but differs quantitatively in that it bends downward somewhat more quickly. Another way to quantify the difference is to compare the predictions for the conductance at the voltage $V = T_K$. As mentioned in the main text, our calculations yield $g(V = T_K) \approx 0.6$, whereas RTRG predicts a value of approximately $2/3$.

Despite this discrepency, we note that if both our and the RTRG conductance curves are plotted versus V/V_K, thus making the comparison independent of the finite-temperature, equilibrium scale T_K, the two curves almost coincide over a wide range of V/V_K values, see Fig. S7(b). This suggests that the reason for the discrepancy in Fig. S7(a) is that the RTRG approach has an inaccuracy of a few percent in its determination of the ratio V_K/T_K.
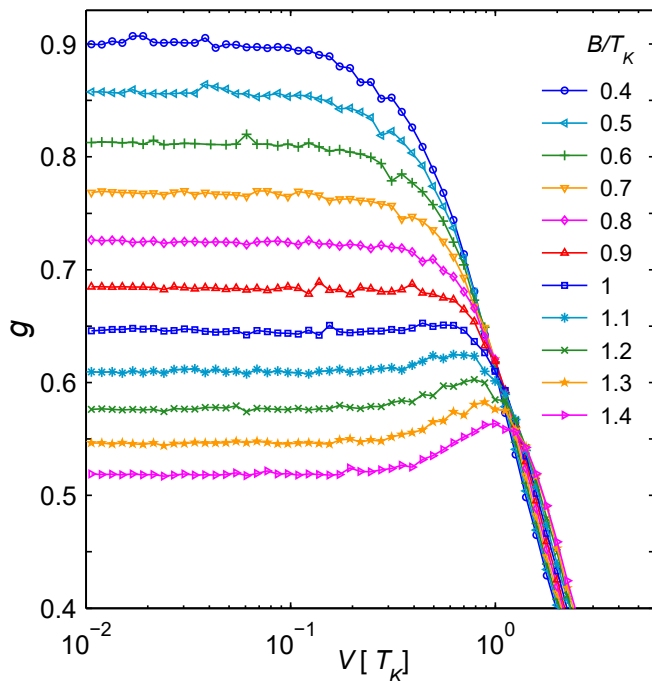
Figure S8. Conductance as a function of voltage at $T = 0$ for different magnetic fields B. We used the same physical parameters as in Fig. 3(c) of the main text, but for more values of the magnetic field B.

S-7. SPLITTING FIELD IN THE SIAM

With increasing magnetic field, the zero-bias peak in the conductance of the SIAM splits into two subpeaks, the position of which is approximately given by $V \approx \pm B$. It has long been of interest to have a quantitatively reliable value for the "splitting field" at which the peak splitting first becomes noticeable. The splitting field can be defined in two ways: (i) as the field B_* at which the number of local maxima changes from one to larger than one; or (ii) as the field B_{**} at which the maximum at zero bias turns into a minimum. In principle, these two fields need not coincide: if two side peaks emerge in the flanks of the zero-bias peak before the central maximum has turned into a minimum, B_* would be smaller than B_{**}. However, we would like to argue this does not occur in the present case, for which the mechanism for the peak splitting is well understood. The zero-bias conductance peak is computed as the sum of two peaks, one for spin up and one for spin down. These are pushed apart with increasing field. Once their spacing becomes comparable to their widths, their sum changes from showing a single to a double maximum, with a local minimum in between. This implies $B_* = B_{**}$. Note, though, that for fields just above B_{**}, the local minimum between the two maxima will still be extremely weak and the curve will look essentially flat there. The two maxima will become discernable as unambiguous "peaks" only at fields somewhat larger than B_{**}. Therefore, if one attempts to

estimate B_* from (noisy) numerical data, by determining the field, say $B_*^{\rm sp}$, at which side peaks (sp) first become clearly noticeable, this will always yield values somewhat larger than $B_* = B_{**}$.

Fig. S8 shows our numerical results for the zero-temperature conductance as a function of voltage for different magnetic fields $B \approx T_K$, for $U/\Gamma = 12$, as in Fig. 3(c-d) of the main text. While the curve for $B/T_K = 1$ exhibits a clear peak for non-zero voltage, this is not the case for $B/T_K = 0.8T_K$, and the curve for $B/T_K = 0.9$ is a bit too noisy to unambigously identify a side peak. We may therefore regard $B_*^{\rm sp} = T_K$ as a conservative upper bound for the actual splitting field. On the other hand, it is not possible to estimate B_{**} from our data. B_{**} is the field at which $-C_V = \left[\frac{\partial^2}{\partial V^2}g(V)\right]_{V=0}$, the curvature of the conductance at zero bias, changes from negative to positive. However, extracting this curvature reliably from our data would require a level of numerical noise on the order of 0.1%, all the more when tuning B such that C_V tends to zero.

Very recently, exact results for C_V and hence B_{**} have become available. Filippone, Moca, von Delft and Mora (FMDM) [52] have pointed out that C_V can be extracted from the magnetic field dependence of the local spin and charge susceptibilities of the SIAM, which can be computed using the Bethe Ansatz. However, the formula which FMDM obtained for C_V was incorrect due to a sign error in their calculations. A correct formula for C_V was first published by Oguri and Hewson [53], who showed that the Fermi-liquid relations discussed by FMDM could also be derived using Ward identities and the analytic and antisymmetry properties of the vertex function of the SIAM. Very recently FMDM reported (see version 2 of [52]) that upon eliminating their sign mistake, their corrected formula for C_V coincides with that of Oguri and Hewson. Moreover, NRG results by A. Weichselbaum, included in Appendix D of version 3 of [52], agree with the corrected FL predictions for C_V. Incidentally, Figs. 8(c,d) of that analysis illustrates why extracting C_V from $g^{T=0}(V)$ would require an accuracy of order 0.1% for the numerical determination of the conductance as function V.

In the Kondo limit $U/\Gamma \gg 1$, FMDM obtained a splitting field of $B_{**} = 0.75073T_K^{(\chi)}$, where $T_K^{(\chi)} = \frac{1}{4\chi_s}$ is the Kondo scale defined via the zero-field, zero-temperature spin susceptibility. As stated in the caption of Fig. 3 of the main text, $T_K^{(\chi)}$ is related to the Kondo temperature used in this work, defined via $g(T=T_K, V=0) = \frac{1}{2}$, by $T_K^{(\chi)} = T_K/1.04$ for the parameters used in Figs. 3 and S8. (For a detailed discussion of various different definitions of T_K, see Ref. [46].) Thus, the Fermi-liquid prediction for the splitting field translates to $B_{**} = 0.72T_K$. The fact that our upper bound estimate, $B_*^{\rm sp} = T_K$, is somewhat but not much larger than this value implies that our results are compatible with the slitting field predictions from Fermi liquid theory.